

# X-ray spectroscopic survey of highly-accreting AGN

M. Laurenti<sup>1,2</sup>, E. Piconcelli<sup>2</sup>, L. Zappacosta<sup>2</sup>, F. Tombesi<sup>1,2,4,5</sup>, C. Vignali<sup>6,7</sup>, S. Bianchi<sup>8</sup>, P. Marziani<sup>9</sup>, F. Vagnetti<sup>1,3</sup>, A. Bongiorno<sup>2</sup>, M. Bischetti<sup>10</sup>, A. del Olmo<sup>11</sup>, G. Lanzuisi<sup>7</sup>, A. Luminari<sup>2,3</sup>, R. Middei<sup>2,12</sup>, M. Perri<sup>2,12</sup>, C. Ricci<sup>13,14</sup>, and G. Vietri<sup>2,15</sup>

<sup>1</sup> Dipartimento di Fisica, Università di Roma “Tor Vergata”, Via della Ricerca Scientifica 1, I-00133 Roma, Italy  
e-mail: marco.laurenti@roma2.infn.it

<sup>2</sup> INAF - Osservatorio Astronomico di Roma, Via Frascati 33, I-00040 Monte Porzio Catone, Italy

<sup>3</sup> INAF - Istituto di Astrofisica e Planetologia Spaziali, Via del Fosso del Cavaliere 100, I-00133 Roma, Italy

<sup>4</sup> Department of Astronomy, University of Maryland, College Park, MD 20742, USA

<sup>5</sup> NASA/Goddard Space Flight Center, Greenbelt, MD 20771, USA

<sup>6</sup> Dipartimento di Fisica e Astronomia “Augusto Righi”, Università degli Studi di Bologna, Via Gobetti 93/2, I-40129 Bologna, Italy

<sup>7</sup> INAF – Osservatorio di Astrofisica e Scienza dello Spazio di Bologna, Via Gobetti 93/3, I-40129 Bologna, Italy

<sup>8</sup> Dipartimento di Matematica e Fisica, Università degli Studi Roma Tre, Via della Vasca Navale 84, I-00146 Roma, Italy

<sup>9</sup> INAF – Osservatorio Astronomico di Padova, Vicolo Osservatorio 5, I-35122 Padova, Italy

<sup>10</sup> INAF - Osservatorio Astronomico di Trieste, via G. B. Tiepolo 11, I-34143 Trieste, Italy

<sup>11</sup> Instituto de Astrofísica de Andalucía, IAA-CSIC, Glorieta de la Astronomía s/n, 18008 Granada, Spain

<sup>12</sup> Space Science Data Center, SSDC, ASI, via del Politecnico snc, 00133 Roma, Italy

<sup>13</sup> Núcleo de Astronomía de la Facultad de Ingeniería, Universidad Diego Portales, Av. Ejército Libertador 441, Santiago 22, Chile

<sup>14</sup> Kavli Institute for Astronomy and Astrophysics, Peking University, Beijing 100871, People’s Republic of China

<sup>15</sup> INAF - Istituto di Astrofisica Spaziale e Fisica Cosmica Milano, Via A. Corti 12, I-20133 Milano, Italy

## ABSTRACT

Improving our understanding of the nuclear properties of high-Eddington ratio ( $\lambda_{\text{Edd}}$ ) active galactic nuclei (AGN) is necessary since at this regime the radiation pressure is expected to affect the structure and efficiency of the accretion disc-corona system. This may cause departures from the typical nuclear properties of low- $\lambda_{\text{Edd}}$  AGN, which have been largely studied so far. We present here the X-ray spectral analysis of 14 radio-quiet,  $\lambda_{\text{Edd}} \geq 1$  AGN at  $0.4 \leq z \leq 0.75$ , observed with *XMM-Newton*. Optical/UV data from simultaneous Optical Monitor observations have been also considered. These quasars have been selected to have relatively high values of black hole mass ( $M_{\text{BH}} \sim 10^{8-8.5} M_{\odot}$ ) and bolometric luminosity ( $L_{\text{bol}} \sim 10^{46}$  erg s<sup>-1</sup>), in order to complement previous studies of high- $\lambda_{\text{Edd}}$  AGN at lower  $M_{\text{BH}}$  and  $L_{\text{bol}}$ . We studied the relation between  $\lambda_{\text{Edd}}$  and other key X-ray spectral parameters, such as the photon index ( $\Gamma$ ) of the power-law continuum, the X-ray bolometric correction  $k_{\text{bol,X}}$  and the optical/UV-to-X-ray spectral index  $\alpha_{\text{ox}}$ . Our analysis reveals that, despite the homogeneous optical and SMBH accretion properties, the X-ray properties of these high- $\lambda_{\text{Edd}}$  AGN are quite heterogeneous. We indeed measured values of  $\Gamma$  comprised between 1.3 and 2.5, at odds with the expectations based on previously reported  $\Gamma - \lambda_{\text{Edd}}$  relations, by which  $\Gamma \geq 2$  would be an ubiquitous hallmark of AGN with  $\lambda_{\text{Edd}} \sim 1$ . Interestingly, we found that  $\sim 30\%$  of the sources are X-ray weak, with an X-ray emission about a factor of  $\sim 10 - 80$  fainter than that of typical AGN at similar UV luminosities. The X-ray weakness seems to be intrinsic and not due to the presence of absorption along the line of sight to the nucleus. This result may indicate that high- $\lambda_{\text{Edd}}$  AGN commonly undergo periods of intrinsic X-ray weakness. Furthermore, results from a follow-up monitoring with *Swift* of one of these X-ray weak sources suggest that these periods can last for several years.

**Key words.** galaxies: active – quasars: general – quasars: supermassive black holes

## 1. Introduction

Active galactic nuclei (AGN) are fuelled by accretion processes onto a central supermassive black hole (SMBH). The AGN accretion activity is usually quantified by the Eddington ratio, which is defined as the ratio between the AGN bolometric luminosity and the Eddington luminosity, i.e.  $\lambda_{\text{Edd}} = L_{\text{bol}}/L_{\text{Edd}}$ . The Eddington ratio is thus intimately connected with the accretion rate  $\dot{M}$ , since  $\lambda_{\text{Edd}} \propto \dot{M}/M_{\text{BH}} \propto \dot{M}/\dot{M}_{\text{Edd}}$ , where  $M_{\text{BH}}$  is the black hole mass,  $\dot{M}_{\text{Edd}} = L_{\text{Edd}}/(\eta c^2)$  and  $\eta$  is the radiative efficiency.

The bulk of the X-ray spectroscopic studies of AGN is focused on local ( $z \lesssim 0.1$ ) sources with low-to-moderate ( $\lesssim 0.3$ )  $\lambda_{\text{Edd}}$  (e.g. Nandra & Pounds 1994; Piconcelli et al. 2005; Bianchi et al. 2009; Ricci et al. 2018). Because of their relative paucity in the local Universe (e.g. Shankar et al. 2013; Shirakata et al.

2019), highly-accreting (i.e.  $\lambda_{\text{Edd}} \gtrsim 0.5$ ) AGN have been largely overlooked so far, with the notable exception of the Narrow Line Seyfert 1 galaxies (NLSy1s; e.g. Brandt et al. 1997; Gallo 2006; Costantini et al. 2007; Jin et al. 2013; Fabian et al. 2013; Waddell & Gallo 2020). However NLSy1s represent a peculiar and restricted class of low-mass ( $10^6 - 10^7 M_{\odot}$ ) AGN with the narrowest permitted emission lines in type-1 AGN samples (FWHM(H $\beta$ )  $< 2000$  km s<sup>-1</sup>; e.g. Osterbrock & Pogge 1985; Marziani et al. 2018, and references therein). In this sense, the NLSy1s may be a biased population, therefore it would be desirable to expand the study of the multi-wavelength properties of high- $\lambda_{\text{Edd}}$  AGN to sources with Balmer lines widths of FWHM  $\geq 2000$  km s<sup>-1</sup> and hosting more massive SMBHs. Past and recent works support a close relation between the prominence of the optical Fe II emission and  $\lambda_{\text{Edd}}$  (e.g. Marziani et al. 2001; Shen & Ho 2014; Dou et al. 2016), with the strong Fe II emission

associated with high Eddington ratio. This result appears to be independent of the line width.

A clear understanding of the nuclear properties of high- $\lambda_{\text{Edd}}$  AGN, regardless of their  $L_{\text{bol}}$  and  $M_{\text{BH}}$ , would be extremely important for several reasons, as detailed as follows. The standard model of accretion discs, developed by [Shakura & Sunyaev \(1973\)](#), predicts an optically thick, geometrically thin disc which is radiatively efficient. While this picture may hold for AGN in the low- $\lambda_{\text{Edd}}$  regime, it is supposed to break down for high- $\lambda_{\text{Edd}}$  sources, as the radiation pressure gains more importance with increasing accretion rate, and the circumnuclear region of the disc thickens vertically. These systems are often called slim discs, as they are both optically- and geometrically-thick (e.g. [Abramowicz et al. 1988](#); [Chen & Wang 2004](#); [Sądowski et al. 2011](#)). Slim discs are also expected to have a low radiative efficiency because of the photon trapping effect. The diffusion timescale of photons in optically- and geometrically-thick discs may be longer than the accretion timescale and they are advected into the central SMBH with the infalling material. This implies that the observed disc luminosity ( $\sim L_{\text{bol}}$ ) and, in turn, the  $\lambda_{\text{Edd}}$  are expected to saturate to a limiting value of approximately  $5 - 10 L_{\text{Edd}}$  for steadily increasing accretion rates (e.g. [Mineshige et al. 2000](#)). However, some critical issues on the theoretical side are still unsolved and the broadband spectral energy distributions of high- and low- $\lambda_{\text{Edd}}$  AGN do not appear to exhibit clear differences (e.g. [Castelló-Mor et al. 2017](#); [Liu et al. 2021](#)).

Furthermore, the study of high- $\lambda_{\text{Edd}}$  AGN is important in terms of their cosmological implications. In fact, in the past few years there has been an increasing effort to detect quasars (i.e. AGN with  $L_{\text{bol}} > 10^{46}$  erg s $^{-1}$ ; QSOs hereafter) shining at  $z \sim 6 - 7$ , when the universe was less than 1 Gyr old (e.g. [Wu et al. 2015](#); [Bañados et al. 2016](#); [Mazzucchelli et al. 2017](#)). The vast majority of these QSOs typically host massive SMBHs (e.g.  $M_{\text{BH}} \geq 10^9 M_{\odot}$ ) and the process that allowed black hole seeds to grow up to billion solar masses in such a relatively short amount of time is still debated. Several scenarios have been proposed (see, e.g., the review in [Valiante et al. 2017](#)) and it has been suggested that these SMBHs may evolve via gas accretion at a rate equal or above the Eddington rate.

Finally, a high  $\lambda_{\text{Edd}}$  is invoked as a key ingredient to launch powerful nuclear outflows (e.g. [Proga 2005](#); [Zubovas & King 2013](#); [King & Pounds 2015](#)) which could be capable of controlling the growth and evolution of the host galaxy (e.g. [Hopkins & Elvis 2010](#); [Fiore et al. 2017](#)). These outflows are believed to deposit large amounts of energy and momentum into the interstellar medium (e.g. [Zubovas & King 2012](#)) and affect the host galaxy gas reservoir available for both star formation and SMBH accretion, offering a possible explanation for the observed  $M_{\text{BH}} - \sigma$  relation (e.g. [Ferrarese & Merritt 2000](#)). Accordingly, the AGN feedback mechanism should manifest itself in full force in high- $\lambda_{\text{Edd}}$  sources, making them the ideal laboratory for probing the real impact of nuclear activity on the evolution of massive galaxies (e.g. [Reeves et al. 2009](#); [Nardini et al. 2015](#); [Tombesi et al. 2015](#); [Marziani et al. 2016](#); [Bischetti et al. 2017](#), 2019; [Laurenti et al. 2021](#)).

The study of the X-ray properties of high- $\lambda_{\text{Edd}}$  AGN allows to enlarge the dynamic range of the relations involving  $\lambda_{\text{Edd}}$  and X-ray spectral parameters and luminosity, by significantly populating the poorly-explored extreme end of the  $\lambda_{\text{Edd}}$  distribution and, thus, imposing crucial constraints on the strength of any possible correlation. A long-standing issue concerning X-ray properties of high- $\lambda_{\text{Edd}}$  AGN is the existence of a correlation between  $\Gamma$  and  $\lambda_{\text{Edd}}$ , whereby a very steep (i.e.  $\Gamma > 2$ ) continuum is a prerogative of sources with  $\lambda_{\text{Edd}} \gtrsim 0.3$  (e.g. [Shemmer et al.](#)

[2008](#); [Risaliti et al. 2009](#); [Brightman et al. 2013](#); [Fanali et al. 2013](#); [Huang et al. 2020](#); [Liu et al. 2021](#)). This correlation has been explained in terms of an enhanced UV emission from the accretion disc due to the high accretion rate, which leads to an increase of the radiative cooling of the X-ray corona (and a decrease of the electron temperature) and, in turn, to a steepening of the emerging X-ray continuum. The discovery of such a strong dependence of  $\Gamma$  on  $\log \lambda_{\text{Edd}}$ , i.e.  $\Gamma \sim 0.3 \times \log \lambda_{\text{Edd}} + 2$  (e.g. [Shemmer et al. 2008](#); [Risaliti et al. 2009](#); [Brightman et al. 2013](#)), has encountered an immediate interest for a possible application in X-ray extragalactic surveys, as it would allow to estimate the SMBH mass of AGN with reliable measurement of  $\Gamma$ , including type-2 AGN, for which commonly-used “single-epoch”  $M_{\text{BH}}$  estimators are not applicable. However, [Trakhtenbrot et al. \(2017\)](#) questioned the existence of a strong correlation between  $\Gamma$  and  $\lambda_{\text{Edd}}$  reporting only a very weak correlation by analyzing a large sample of low- $z$  ( $0.01 < z < 0.5$ ) sources with broadband X-ray spectra from the BAT AGN Spectroscopic Survey.

In addition, [Lusso et al. \(2010\)](#) studied the hard X-ray bolometric correction,  $k_{\text{bol,X}} = L_{\text{bol}}/L_{2-10\text{keV}}$ , and the optical/UV to X-ray spectral slope  $\alpha_{\text{ox}}$  of AGN in the COSMOS survey as a function of  $\log \lambda_{\text{Edd}}$ . They claimed for the existence of a linear relation between the logarithm of the Eddington ratio and the two X-ray quantities. Although affected by large scatter, these relations lend support to a more physically-motivated scenario for the increase of  $k_{\text{bol,X}}$  as a function of  $L_{\text{bol}}$  ([Marconi et al. 2004](#); [Martocchia et al. 2017](#); [Duras et al. 2020](#)) which suggests an X-ray corona-accretion disc system with different properties in the most luminous (i.e. highly-accreting) AGN, producing a relatively weaker X-ray emission (as compared to the optical-UV emission from the accretion disc) than in “standard” AGN. A more refined description of the  $k_{\text{bol,X}} - \lambda_{\text{Edd}}$  relation has been recently provided by [Duras et al. \(2020\)](#), who found  $k_{\text{bol,X}} \propto (\lambda_{\text{Edd}})^{0.61}$  once a sizeable number of highly-accreting QSOs at  $z \sim 2 - 4$  was included. However, a full understanding of the quantitative behaviour of these relations, along with the  $\Gamma - \lambda_{\text{Edd}}$  one, and possible trends with  $M_{\text{BH}}$  or  $L_{\text{bol}}$  is still hampered by the lack of a large number of sources at  $\lambda_{\text{Edd}} \gtrsim 0.9$ . Indeed, the bulk of AGN that have been considered so far are accreting at low-to-moderate  $\lambda_{\text{Edd}}$  regimes ( $\lesssim 0.3$ ).

To mitigate this bias, we present the X-ray spectroscopy of a sample of QSOs outside the local Universe ( $z > 0.1$ ) with  $\lambda_{\text{Edd}} \gtrsim 1$  and  $M_{\text{BH}}$  exceeding  $\sim 10^8 M_{\odot}$ . This paper is organised as follows. We describe the general properties of our sample in Sect. 2, as well as the *XMM-Newton* observations and data reduction. Spectral fits in the X-ray band and optical/UV photometry are detailed in Sect. 3. We then present our results in Sect. 4, which are discussed in Sect. 5. A  $\Lambda$ CDM cosmology ( $H_0 = 67.7$  km s $^{-1}$  Mpc $^{-1}$ ,  $\Omega_{\text{m}} = 0.307$ ,  $\Omega_{\Lambda} = 0.693$ ) from *Planck* 2015 data is adopted throughout the paper ([Planck Collaboration et al. 2016](#)). All errors are quoted at 68% confidence level ( $\Delta C = 1$ ; [Avni 1976](#); [Cash 1979](#)).

## 2. Observations and data reduction

In this work we present the *XMM-Newton* ([Jansen et al. 2001](#)) observations of a sample of 14 AGN drawn from a larger sample of high- $\lambda_{\text{Edd}}$  radio-quiet QSOs reported in [Marziani & Sulentic \(2014\)](#), hereinafter MS14. Specifically, they collected a sample of 43 radio-quiet QSOs in the range  $z \sim 0.4 - 0.75$  with H $\beta$  coverage from a good-quality SDSS spectrum (see Table 1 in MS14). This ensures an accurate measure of  $M_{\text{BH}}$  and, in turn,  $\lambda_{\text{Edd}}$ , being the full width at half maximum (FWHM) of the H $\beta$  emission line a more reliable single-epoch  $M_{\text{BH}}$  estimator than the FWHM

**Table 1:** *XMM-Newton* sample of high- $\lambda_{\text{Edd}}$  QSOs and their general properties.

| Obj. ID  | SDSS Name           | RA          | Dec          | $z$   | $\log(L_{\text{bol}}/\text{erg s}^{-1})$ | $\log(M_{\text{BH}}/M_{\odot})$ | $\lambda_{\text{Edd}}$ | $N_{\text{H,gal}}$ |
|----------|---------------------|-------------|--------------|-------|--|---------------------------------|------------------------|--------------------|
| (1)      | (2)                 | (3)         | (4)          | (5)   | (6)                                      | (7)                             | (8)                    | (9)                |
| J0300–08 | J030000.01–080356.9 | 03 00 00.01 | –08 03 56.90 | 0.562 | 46.5                                     | 8.4                             | 1.1                    | 5.93               |
| J0809+46 | J080908.13+461925.6 | 08 09 08.10 | +46 19 25.30 | 0.657 | 46.5                                     | 8.5                             | 0.9                    | 3.60               |
| J0820+23 | J082024.21+233450.4 | 08 20 24.20 | +23 34 50.20 | 0.47  | 46.0                                     | 7.9                             | 1.0                    | 3.88               |
| J0940+46 | J094033.75+462315.0 | 09 40 33.80 | +46 23 15.00 | 0.696 | 46.4                                     | 8.3                             | 1.1                    | 1.06               |
| J1048+31 | J104817.98+312905.8 | 10 48 18.00 | +31 29 05.80 | 0.452 | 46.2                                     | 8.1                             | 1.0                    | 2.13               |
| J1103+41 | J110312.93+414154.9 | 11 03 12.00 | +41 41 55.00 | 0.402 | 46.4                                     | 8.3                             | 1.0                    | 0.81               |
| J1127+11 | J112756.76+115427.1 | 11 27 56.80 | +11 54 27.00 | 0.51  | 46.3                                     | 8.1                             | 1.1                    | 3.17               |
| J1127+64 | J112757.41+644118.4 | 11 27 57.40 | +64 41 18.20 | 0.695 | 46.4                                     | 8.2                             | 1.2                    | 0.79               |
| J1206+41 | J120633.07+412536.1 | 12 06 33.10 | +41 25 35.80 | 0.554 | 46.3                                     | 8.3                             | 0.9                    | 1.60               |
| J1207+15 | J120734.62+150643.6 | 12 07 34.60 | +15 06 43.60 | 0.75  | 46.5                                     | 8.4                             | 0.9                    | 2.26               |
| J1218+10 | J121850.51+101554.1 | 12 18 50.50 | +10 15 54.00 | 0.543 | 46.2                                     | 8.0                             | 1.2                    | 1.72               |
| J1245+33 | J124511.25+335610.1 | 12 45 11.30 | +33 56 10.10 | 0.711 | 46.6                                     | 8.5                             | 1.1                    | 1.20               |
| J1301+59 | J130112.93+590206.7 | 13 01 12.93 | +59 02 06.70 | 0.476 | 46.7                                     | 8.5                             | 1.2                    | 1.40               |
| J1336+17 | J133602.01+172513.0 | 13 36 02.00 | +17 25 13.10 | 0.552 | 46.6                                     | 8.5                             | 0.9                    | 1.64               |

**Notes:** (1) Abbreviated object ID; (2) SDSS IAU name; (3) right ascension (hours); (4) declination (degrees); (5) redshift from MS14; (6) bolometric luminosity (typical error of  $< 0.2$  dex) from the [Runnoe et al. \(2012\)](#) relation; (7) black hole mass (typical error of  $0.3 - 0.4$  dex; see e.g. [Rakshit et al. 2020](#)) from the [Vestergaard & Peterson \(2006\)](#) single-epoch virial relation; (8) Eddington ratio; (9) Galactic column density ( $10^{20} \text{ cm}^{-2}$ ) from the full-sky H I map by [HI4PI Collaboration et al. \(2016\)](#).

of C IV (e.g. [Baskin & Laor 2005](#); [Vietri et al. 2018, 2020](#)), which is typically used for QSOs at  $z \gg 1$ . The  $M_{\text{BH}}$  of these MS14 QSOs are in the range  $10^{8-8.5} M_{\odot}$ , while their  $L_{5100\text{\AA}}$ -based  $L_{\text{bol}}$  are clustered around a few  $10^{46} \text{ erg s}^{-1}$ , with  $\lambda_{\text{Edd}}$  values spanning from  $\sim 0.5$  to  $\sim 2$ . Such highly-accreting objects are also characterised by strong Fe II emission with  $R_{\text{Fe II}} = \text{EW}(\text{Fe II } \lambda 4570)/\text{EW}(\text{H}\beta) > 1$ , and MS14 dubbed them as extreme Population A (xA) QSOs. For our *XMM-Newton* observing program, we considered the 14 xA QSOs from the MS14 sample with  $\lambda_{\text{Edd}} \gtrsim 1$  and an estimated  $L_{\text{bol}} \geq 10^{46} \text{ erg s}^{-1}$ .

The main properties of our high- $\lambda_{\text{Edd}}$  QSO sample are listed in Tab. 1. The bolometric luminosities are calculated by adopting the relation  $\log L_{\text{bol}} = 4.891 + 0.912 \log(\lambda L_{\lambda})$ , with  $\lambda = 5100 \text{ \AA}$ , from [Runnoe et al. \(2012\)](#). The  $M_{\text{BH}}$  are estimated by using the single-epoch virial relation based on the FWHM of the H $\beta$  and the monochromatic luminosity at  $\lambda = 5100 \text{ \AA}$ , as described by [Vestergaard & Peterson \(2006\)](#):  $\log M_{\text{BH}}(\text{H}\beta) = \log[\text{FWHM}/1000 \text{ km s}^{-1}]^2 + \log[\lambda L_{\lambda}/10^{44} \text{ erg s}^{-1}]^{0.5} + 6.91$ . The virial mass estimates based on single-epoch spectra are typically dominated by the systematic uncertainty of  $\sim 0.3 - 0.4$  dex (e.g. [Collin et al. 2006](#); [Shen 2013](#); [Rakshit et al. 2020](#)), while the uncertainty associated with the [Runnoe et al. \(2012\)](#) relation for  $\log L_{\text{bol}}$  is smaller than 0.2 dex for the median value of  $L_{5100\text{\AA}} \sim 7 \times 10^{41} \text{ erg s}^{-1} \text{ \AA}^{-1}$  of our sample. The errors on  $\log M_{\text{BH}}$  and  $\log L_{\text{bol}}$  then propagate to uncertainties in  $\log \lambda_{\text{Edd}}$ .

*XMM-Newton* observed 12 out of the 14 high- $\lambda_{\text{Edd}}$  AGN during the AO 18 Cycle campaign (PI: E. Piconcelli). The remaining two sources, namely J1301+59 and J0300–08, had publicly available *XMM-Newton* observations at the time of our investigation. Detailed information on the *XMM-Newton* data for

each source in the sample are listed in Tab. 2. Raw data from all sources have been retrieved from the *XMM-Newton* Science Archive and then processed using the *XMM-Newton* Science Analysis System (SAS v18.0.0) with the latest available calibration files. We take advantage of the full potential of *XMM-Newton* in the X-ray energy interval  $E = 0.3 - 10 \text{ keV}$  (observer-frame) by collecting data by its primary instrument, i.e. the European Photon Imaging Camera *EPIC*, equipped with the three X-ray CCD cameras, namely the pn ([Strüder et al. 2001](#)) and the two MOS detectors ([Turner et al. 2001](#)). Data reduction, filtering of high background periods and spectral extraction were performed according to the standard procedures described in the SAS web page<sup>1</sup>. For each object, we chose a circular region of radius  $\sim 10 - 20 \text{ arcsec}$  for the source extraction, and a nearby, larger source-free circular region for the background. The spectra were binned to ensure at least one count per bin and modelled within the XSPEC v12.11.1c package by minimising the C-statistic ([Cash 1979](#)).

In addition, our study is complemented with the analysis of the simultaneous optical/UV data taken with the Optical Monitor (OM; [Mason et al. 2001](#)). Raw OM data are converted into science products by using the SAS task `omchain`. We use the task `om2pha` to convert the OM photometric points into a suitable format for XSPEC ([Arnaud 1996](#)).

<sup>1</sup> <https://www.cosmos.esa.int/web/xmm-newton/sas-threads>.

**Table 2:** Journal of the *XMM-Newton* observations.

| Obj. ID  | Obs. ID    | $t_{\text{net}}$ | $E _{\text{h}}$ | cts $_{\text{bb}}$ (cts $_{\text{h}}$ ) |
|----------|------------|------------------|-----------------|---|
| (1)      | (2)        | (3)              | (4)             | (5)                                     |
| J0300–08 | 0802220401 | 33.1/44.9/45.5   | 1.28            | 74/14/34 (24/4/9)                       |
| J0809+46 | 0843830101 | 11.5/16.3/16.4   | 1.21            | 323/93/108 (187/59/73)                  |
| J0820+23 | 0843830201 | 9.9/16.4/16.4    | 1.36            | 507/223/244 (114/63/74)                 |
| J0940+46 | 0843830301 | 13.0/19.4/19.5   | 1.18            | 1831/505/469 (224/94/84)                |
| J1048+31 | 0843830401 | 8.5/16.4/16.4    | 1.38            | 392/183/203 (172/89/118)                |
| J1103+41 | 0843830501 | 13.7/16.8/16.8   | 1.43            | 999/269/270 (161/57/63)                 |
| J1127+11 | 0843830601 | 2.5/12.5/13.8    | 1.32            | 380/504/568 (69/138/145)                |
| J1127+64 | 0843830701 | 16.5/24.7/24.7   | 1.18            | 51/20/30 (8/5/15)                       |
| J1206+41 | 0843830801 | 4.1/10.9/11.7    | 1.29            | 230/114/112 (26/24/32)                  |
| J1207+15 | 0843830901 | 10.8/16.4/16.4   | 1.14            | 948/331/321 (298/146/137)               |
| J1218+10 | 0843831001 | 4.1/18.7/17.8    | 1.30            | 449/340/445 (54/68/64)                  |
| J1245+33 | 0843831101 | 12.1/16.1/16.1   | 1.17            | 58/15/13 (22/6/4)                       |
| J1301+59 | 0304570101 | 8.5/11.2/12.1    | 1.36            | 4037/1336/1297 (696/337/339)            |
| J1336+17 | 0843831201 | 4.8/11.8/11.8    | 1.29            | 1801/1070/1205 (574/479/546)            |

**Notes:** (1) Abbreviated object ID; (2) *XMM-Newton* observation ID; (3) net exposure for the pn/MOS1/MOS2 cameras (ks); (4) lower observer-frame bound of the hard X-ray energy range adopted to constrain the slope of the underlying primary continuum,  $E|_{\text{h}} = 2/(1+z)$  energy (keV); (5) net counts of the pn/MOS1/MOS2 cameras in the broadband (hard)  $E = 0.3 - 10$  keV ( $E > 2$  keV rest frame) observer-frame energy interval.

### 3. Data analysis

#### 3.1. X-ray spectroscopy

We adopted the following procedure to analyse the X-ray spectrum of each source in our sample. Data from *EPIC*-pn, MOS1 and MOS2 were always considered simultaneously and fitted together, taking into account an intercalibration constant ( $< 10\%$ ) between the three instruments. We first ignored all the data outside the  $E = 0.3 - 10$  keV observer-frame energy interval. Initially, only data in the intrinsic hard X-ray range, i.e. with  $E > 2$  keV in the rest frame of the source, corresponding to  $E > 2/(1+z)$  keV in the observer frame, were considered. This hard X-ray portion of the spectrum was modelled with a power law modified by Galactic absorption to constrain the slope of the underlying primary continuum without any contamination from the likely soft excess component emerging at lower energies, which may strongly affect the measurement of the photon index  $\Gamma$ . From this simple spectral fit, we found the bulk of  $\Gamma$  values to be comprised between  $\sim 1.7$  and  $2.3$ , which is the typical range of radio-quiet AGN (e.g. Piconcelli et al. 2005; Gliozzi & Williams 2020). A flatter hard-band continuum (i.e.  $\Gamma \sim 1.2 - 1.3$ ) was found for two sources, namely J1048+31 and J1245+33, although the latter was affected by large uncertainty. Finally, the  $\Gamma$  value of J0300–08 resulted basically unconstrained due to the limited statistics.

We then extended our spectral analysis to the whole  $E = 0.3 - 10$  keV energy interval by including the soft X-ray portion. The extrapolation of the model to soft energies showed for all but one sources (J0809+46)<sup>2</sup> the presence of a soft ex-

cess component in their X-ray spectra and we tried to model this feature by considering two different spectral components, i.e., a blackbody or an additional power law, both modified by Galactic absorption. Clearly, we are aware that both models merely provide a phenomenological explanation of the soft excess, whose physical origin is still debated (e.g. Sobolewska & Done 2007; Fukumura et al. 2016; Petrucci et al. 2018; Middei et al. 2020). However, the blackbody model provided the best description of the soft excess in terms of C-statistic for all the spectra.

From our broadband spectral analysis we obtained the best-fit values of the photon index  $\Gamma$  and the blackbody temperature  $kT_{\text{bb}}$  as listed in Tab. 3. We find that our high- $\lambda_{\text{Edd}}$  AGN do have  $kT_{\text{bb}}$  which are consistent with those typically measured for type-1 AGN (e.g. Piconcelli et al. 2005; Bianchi et al. 2009). For two sources, J1245+33 and J0300–08, we fixed the photon index of the power-law component due to the limited quality of spectral data. Specifically, for J1245+33 we fixed  $\Gamma = 1.3$ , which is the value derived from power-law fit to the hard X-ray portion of the spectrum, while for J0300–08 we adopted the canonical value of  $\Gamma = 1.9$  found for radio-quiet quasars in previous works (e.g. Reeves & Turner 2000; Piconcelli et al. 2005), since the photon index was largely unconstrained in this case. No significant evidence for Fe  $K\alpha$  emission was found in the spectra, except for J1048+31, for which we report the presence of an emission line at  $E = 6.52_{-0.04}^{+0.05}$  keV with a rest-frame equivalent width of  $EW = 400_{-140}^{+150}$  eV (see Fig. A.1 of Appendix A). Also shown in Fig. A.1 are the X-ray spectra, and the corresponding best fit, of all the 14 high- $\lambda_{\text{Edd}}$  AGN analysed in this

source shows no soft excess: at low energies its spectrum is dominated by an ionised absorption component with high column density (see Fig. A.1).

<sup>2</sup> A detailed spectral analysis of J0809+46 will be presented in a forthcoming paper (Piconcelli et al., *in prep.*). The X-ray spectrum of this

**Table 3:** Best-fitting spectral parameters for the broadband ( $E = 0.3 - 10$  keV) X-ray spectra of each sample source, measured by assuming a model consisting of a power law plus a blackbody component, modified by Galactic absorption.

| Obj. ID               | $\Gamma$        | $kT_{\text{bb}}$  | (C-stat/d.o.f.) (d.o.f.) | $F_{0.5-2\text{keV}}$                  | $F_{2-10\text{keV}}$                | $L_{0.5-2\text{keV}}$                 | $L_{2-10\text{keV}}$               | $k_{\text{bol,X}}$     | $R_{\text{S/P}}$ |
|-----------------------|-----------------|-------------------|--------------------------|--|-------------------------------------|---------------------------------------|------------------------------------|------------------------|------------------|
| (1)                   | (2)             | (3)               | (4)                      | (5)                                    | (6)                                 | (7)                                   | (8)                                | (9)                    | (10)             |
| J0300-08              | 1.9 (fixed)     | $140 \pm 30$      | 1.22 (60)                | $3.7_{-0.7}^{+0.3} \times 10^{-15}$    | $4.3_{-0.5}^{+0.9} \times 10^{-15}$ | $9.4_{-0.7}^{+0.8} \times 10^{42}$    | $6_{-1}^{+1} \times 10^{42}$       | $5100 \pm 2500$        | 1.24             |
| J0809+46 <sup>a</sup> | $2.10 \pm 0.06$ | –                 | 1.16 (169)               | $2.8_{-0.2}^{+0.1} \times 10^{-14}$    | $8.6_{-0.9}^{+0.7} \times 10^{-14}$ | $2.4_{-0.4}^{+0.3} \times 10^{44}$    | $2.3_{-0.4}^{+0.2} \times 10^{44}$ | $150 \pm 70$           | –                |
| J0820+23              | $2.26 \pm 0.09$ | $80 \pm 20$       | 1.08 (173)               | $8.3_{-0.6}^{+0.3} \times 10^{-14}$    | $7.1_{-0.6}^{+0.5} \times 10^{-14}$ | $1.13_{-0.07}^{+0.07} \times 10^{44}$ | $6.9_{-0.5}^{+0.5} \times 10^{43}$ | $150 \pm 70$           | 0.28             |
| J0940+46              | $2.3 \pm 0.1$   | $134 \pm 4$       | 0.90 (205)               | $1.18_{-0.03}^{+0.03} \times 10^{-13}$ | $5.3_{-0.6}^{+0.5} \times 10^{-14}$ | $6.7_{-0.2}^{+0.2} \times 10^{44}$    | $1.4_{-0.2}^{+0.2} \times 10^{44}$ | $200 \pm 90$           | 2.59             |
| J1048+31 <sup>b</sup> | $1.27 \pm 0.08$ | $120 \pm 20$      | 0.81 (210)               | $5.1_{-0.4}^{+0.2} \times 10^{-14}$    | $1.8_{-0.2}^{+0.2} \times 10^{-13}$ | $4.4_{-0.3}^{+0.3} \times 10^{43}$    | $1.1_{-0.1}^{+0.1} \times 10^{44}$ | $140 \pm 70$           | 0.55             |
| J1103+41              | $1.6 \pm 0.1$   | $122 \pm 6$       | 0.84 (196)               | $6.9_{-0.2}^{+0.2} \times 10^{-14}$    | $7.7_{-0.9}^{+0.7} \times 10^{-14}$ | $6.9_{-0.3}^{+0.3} \times 10^{43}$    | $4.1_{-0.5}^{+0.6} \times 10^{43}$ | $600 \pm 300$          | 2.42             |
| J1127+11              | $2.3 \pm 0.1$   | $170 \pm 20$      | 0.91 (192)               | $2.24_{-0.06}^{+0.05} \times 10^{-13}$ | $1.4_{-0.2}^{+0.2} \times 10^{-13}$ | $3.6_{-0.3}^{+0.4} \times 10^{44}$    | $1.7_{-0.3}^{+0.3} \times 10^{44}$ | $100 \pm 50$           | 0.52             |
| J1127+64              | $1.5 \pm 0.4$   | $110 \pm 20$      | 0.77 (53)                | $3.8_{-1.3}^{+0.2} \times 10^{-15}$    | $7_{-4}^{+2} \times 10^{-15}$       | $2.4_{-0.7}^{+0.3} \times 10^{43}$    | $1.2_{-0.5}^{+0.7} \times 10^{43}$ | $2000_{-1300}^{+1500}$ | 4.37             |
| J1206+41              | $1.4 \pm 0.2$   | $128 \pm 7$       | 0.70 (97)                | $6.2_{-0.5}^{+0.2} \times 10^{-14}$    | $8_{-2}^{+2} \times 10^{-14}$       | $1.90_{-0.07}^{+0.09} \times 10^{44}$ | $8_{-2}^{+2} \times 10^{43}$       | $300 \pm 100$          | 5.52             |
| J1207+15              | $2.0 \pm 0.1$   | $160_{-50}^{+30}$ | 0.97 (224)               | $1.04_{-0.03}^{+0.02} \times 10^{-13}$ | $1.1_{-0.1}^{+0.1} \times 10^{-13}$ | $3.9_{-0.4}^{+0.4} \times 10^{44}$    | $3.1_{-0.4}^{+0.5} \times 10^{44}$ | $100 \pm 50$           | 0.45             |
| J1218+10              | $2.5 \pm 0.2$   | $160 \pm 10$      | 0.98 (162)               | $1.43_{-0.04}^{+0.05} \times 10^{-13}$ | $5.1_{-0.8}^{+0.6} \times 10^{-14}$ | $3.1_{-0.3}^{+0.3} \times 10^{44}$    | $8_{-2}^{+2} \times 10^{43}$       | $200 \pm 100$          | 0.97             |
| J1245+33              | 1.3 (fixed)     | $120 \pm 20$      | 0.96 (44)                | $5.2_{-1.0}^{+0.4} \times 10^{-15}$    | $1.3_{-0.2}^{+0.2} \times 10^{-14}$ | $2.6_{-0.1}^{+0.3} \times 10^{43}$    | $2.1_{-0.4}^{+0.4} \times 10^{43}$ | $2000 \pm 1000$        | 2.93             |
| J1301+59              | $2.01 \pm 0.05$ | $122 \pm 3$       | 0.98 (295)               | $4.65_{-0.09}^{+0.06} \times 10^{-13}$ | $3.9_{-0.2}^{+0.2} \times 10^{-13}$ | $7.0_{-0.2}^{+0.2} \times 10^{44}$    | $3.6_{-0.2}^{+0.2} \times 10^{44}$ | $140 \pm 60$           | 1.25             |
| J1336+17              | $1.86 \pm 0.04$ | $100_{-30}^{+40}$ | 1.01 (336)               | $4.3_{-0.1}^{+0.1} \times 10^{-13}$    | $6.4_{-0.2}^{+0.2} \times 10^{-13}$ | $6.0_{-0.2}^{+0.2} \times 10^{44}$    | $7.8_{-0.3}^{+0.3} \times 10^{44}$ | $50 \pm 20$            | 0.10             |

**Notes:** (1) Abbreviated object ID; (2) photon index of the power-law continuum component; (3) rest-frame temperature of the blackbody component (eV); (4) ratio between the C-stat value of the spectral fit and the degrees of freedom; (5) flux in the 0.5 – 2 keV band ( $\text{erg cm}^{-2} \text{s}^{-1}$ ); (6) flux in the 2 – 10 keV band ( $\text{erg cm}^{-2} \text{s}^{-1}$ ); (7) luminosity in the 0.5 – 2 keV band ( $\text{erg s}^{-1}$ ); (8) luminosity in the 2 – 10 keV band ( $\text{erg s}^{-1}$ ); (9) X-ray bolometric correction; (10) value of the  $R_{\text{S/P}}$  parameter. <sup>a</sup> the best-fit model of J0809+46 is a power law modified by a warm absorber component (see Sect. 3.1 and Fig. A.1 of Appendix A) and it does not require a blackbody component. <sup>b</sup> the best-fit model of J1048+31 also includes a Gaussian emission line component, see Fig. A.1 of Appendix A.

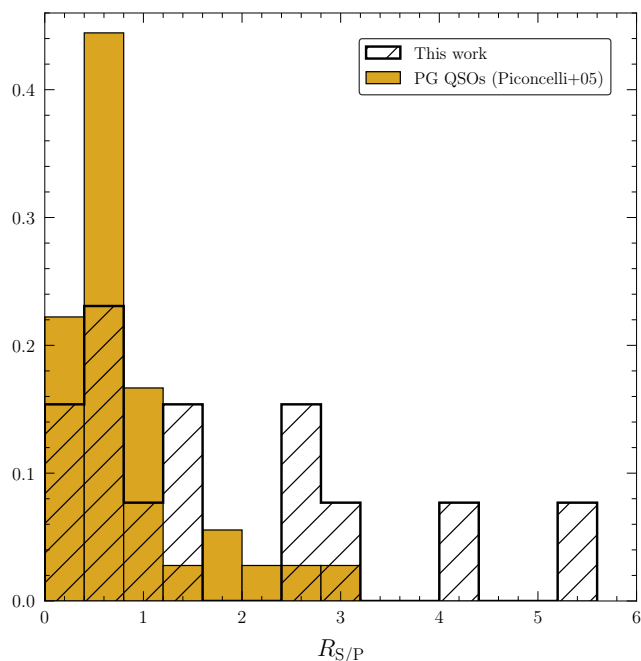


**Fig. 1:** Distribution of  $R_{\text{S/P}} = L_{\text{BB}}^{0.5-2\text{keV}} / L_{\text{PL}}^{0.5-2\text{keV}}$  for our AGN sample (in black) and the sample of PG QSOs from Piconcelli et al. (2005) (in gold).  $R_{\text{S/P}}$  measures the relative strength between the luminosity of the blackbody and power law component in the  $E = 0.5 - 2$  keV energy band.

work. Moreover, in Appendix B (see also Fig. B.1) we present the results of the X-ray spectral analysis of some interesting serendipitous sources located in the *XMM-Newton* field of view of our targeted high- $\lambda_{\text{Edd}}$  AGN. Table 3 also lists the values of the flux and luminosity of the 14 high- $\lambda_{\text{Edd}}$  QSOs in both the

soft ( $E = 0.5 - 2$  keV) and the hard X-ray ( $E = 2 - 10$  keV) band, as well as the X-ray bolometric correction  $k_{\text{bol,X}}$  resulting from this broadband spectral fit. Furthermore, we also calculated the parameter  $R_{\text{S/P}} = L_{\text{BB}}^{0.5-2\text{keV}} / L_{\text{PL}}^{0.5-2\text{keV}}$  which is a proxy of the relative strength between the luminosity of the blackbody and power law components (i.e. the soft excess and the primary continuum, respectively) in the  $E = 0.5 - 2$  keV observer-frame energy band. Figure 1 shows the distribution of  $R_{\text{S/P}}$  for our sample of high- $\lambda_{\text{Edd}}$  AGN compared to that derived by Piconcelli et al. (2005) for a sample of Palomar-Green (PG) QSOs with  $-1.2 \leq \log \lambda_{\text{Edd}} \leq 0.7$ . Such a sample of PG QSOs contains 38 bright objects<sup>3</sup> with an absolute magnitude  $M_B < -23$  in the Johnson’s *B* band, and with redshift  $z \lesssim 1.5$ , which is broadly comparable to that of our high- $\lambda_{\text{Edd}}$  AGN. It is worth noting that the distribution of  $R_{\text{S/P}}$  for the PG QSOs does not extend to values larger than  $\sim 3$  and is largely dominated by sources with  $R_{\text{S/P}} < 1$ , while for our sample the distribution appears smoother and much broader, by reaching values of  $R_{\text{S/P}} \sim 6$ .

### 3.2. Optical/UV photometry

Each source in the sample has at least two available measurements of optical/UV photometry taken with the OM, which are simultaneous to the X-ray data, with one always collected in the *UVWI* (2910 Å) filter.

The other photometric points are distributed among the *B* (4500 Å), *U* (3400 Å), *UVM2* (2310 Å), and *UVW2* (2120 Å) filters. The extinction-corrected optical/UV fluxes are derived as follows. We first consider the optical spectrum of each source from the Sloan Digital Sky Survey (SDSS; York et al. 2000) Legacy campaign. These spectra are the same used by MS14 and

<sup>3</sup> We do not consider PG 1226+023, aka 3C 273, and PG 1115+080: the former is a well-known blazar-line AGN, while the latter is a lensed QSO at redshift  $z \sim 1.7$ .

**Table 4:** Optical/UV properties of the QSOs. Monochromatic luminosities, corrected for both Galactic and local dust extinction, are reported in units of  $10^{30}$  erg  $s^{-1}$  Hz $^{-1}$ .

| Obj. ID  | $E(B - V)_{\text{int}}$ | $L_B$           | $L_U$            | $L_{UVW1}$       | $L_{UVM2}$       | $L_{UVW2}$    | $L_{2500\text{\AA}}$ | $\alpha_{\text{ox}}$ |
|----------|-------------------------|-----------------|------------------|------------------|------------------|---------------|----------------------|----------------------|
| (1)      | (2)                     | (3)             | (4)              | (5)              | (6)              | (7)           | (8)                  | (9)                  |
| J0300–08 | < 0.01                  | –               | $5.68 \pm 0.05$  | $5.54 \pm 0.04$  | $4.6 \pm 0.1$    | $4.2 \pm 0.1$ | $5.78 \pm 0.05$      | $-2.28 \pm 0.03$     |
| J0809+46 | < 0.01                  | $14.6 \pm 0.1$  | $13.7 \pm 0.1$   | $14.0 \pm 0.1$   | –                | –             | $14.3 \pm 0.1$       | $-1.78 \pm 0.02$     |
| J0820+23 | < 0.01                  | $1.91 \pm 0.06$ | $1.57 \pm 0.04$  | $1.61 \pm 0.03$  | –                | –             | $1.65 \pm 0.04$      | $-1.60 \pm 0.01$     |
| J0940+46 | 0.06                    | $4.82 \pm 0.09$ | $4.11 \pm 0.06$  | $4.02 \pm 0.07$  | –                | –             | $4.66 \pm 0.08$      | $-1.65 \pm 0.02$     |
| J1048+31 | 0.20                    | $2.54 \pm 0.08$ | $1.87 \pm 0.06$  | $1.73 \pm 0.06$  | –                | –             | $1.99 \pm 0.05$      | $-1.71 \pm 0.02$     |
| J1103+41 | 0.05                    | $4.89 \pm 0.04$ | $4.29 \pm 0.03$  | $3.80 \pm 0.04$  | –                | –             | $4.33 \pm 0.03$      | $-1.94 \pm 0.02$     |
| J1127+11 | < 0.01                  | –               | $2.47 \pm 0.03$  | $2.41 \pm 0.04$  | $2.33 \pm 0.06$  | –             | $2.51 \pm 0.03$      | $-1.51 \pm 0.02$     |
| J1127+64 | < 0.01                  | $4.14 \pm 0.07$ | $3.49 \pm 0.05$  | $3.39 \pm 0.05$  | –                | –             | $3.99 \pm 0.06$      | $-2.16 \pm 0.04$     |
| J1206+41 | 0.08                    | –               | $1.79 \pm 0.04$  | $1.52 \pm 0.03$  | –                | –             | $2.01 \pm 0.05$      | $-1.73 \pm 0.04$     |
| J1207+15 | 0.13                    | $5.2 \pm 0.2$   | $4.7 \pm 0.1$    | $3.8 \pm 0.1$    | –                | –             | $5.1 \pm 0.2$        | $-1.57 \pm 0.02$     |
| J1218+10 | < 0.01                  | $5.38 \pm 0.07$ | –                | $3.45 \pm 0.04$  | –                | –             | $4.60 \pm 0.05$      | $-1.71 \pm 0.03$     |
| J1245+33 | < 0.01                  | $10.5 \pm 0.1$  | $10.32 \pm 0.09$ | $9.9 \pm 0.1$    | –                | –             | $10.5 \pm 0.1$       | $-2.25 \pm 0.04$     |
| J1301+59 | < 0.01                  | –               | $12.51 \pm 0.03$ | $12.34 \pm 0.04$ | $12.17 \pm 0.06$ | –             | $12.58 \pm 0.03$     | $-1.70 \pm 0.01$     |
| J1336+17 | < 0.01                  | $10.1 \pm 0.1$  | $9.02 \pm 0.08$  | $8.9 \pm 0.1$    | –                | –             | $9.49 \pm 0.09$      | $-1.55 \pm 0.01$     |

**Notes:** (1) Abbreviated object ID; (2) internal reddening; (3)  $B$  rest-frame luminosity; (4)  $U$  rest-frame luminosity; (5)  $UVW1$  rest-frame luminosity; (6)  $UVM2$  rest-frame luminosity; (7)  $UVW2$  rest-frame luminosity; (8) 2500 Å rest-frame luminosity; (9)  $\alpha_{\text{ox}}$ .

were downloaded from the SDSS SkyServer web tool<sup>4</sup>. Galactic extinction is taken into account by considering the color excess measurement from the reddening map of [Schlafly & Finkbeiner \(2011\)](#), provided by the NASA/IPAC Infrared Science Archive (IRSA) website<sup>5</sup>. The spectra are then corrected for Galactic extinction according to the Milky Way reddening law of [Fitzpatrick \(1999\)](#), assuming  $R_V = 3.1$ .

We estimate the possible contribution of the host galaxy starlight to the UV/optical emission by modelling the optical spectrum as a combination of AGN and galaxy components, following the procedure described in [Vagnetti et al. \(2013\)](#). We find that the host galaxy contribution is completely negligible for  $\sim 80\%$  of the sample. For the remaining sources (i.e. J1048+31, J1206+41 and J1218+10), this host galaxy contribution results only to be marginal ( $\lesssim 10\%$ ) and can be ignored.

Furthermore, we look for indications of internal reddening by comparing the SDSS spectra with two different templates: (i) the SDSS composite QSO spectrum by [Vanden Berk et al. \(2001\)](#); and (ii) a median composite spectrum of xA QSOs built from the full sample of highly-accreting QSOs in MS14 (see also [Marziani et al., in prep.](#)). For each source, the SDSS spectrum and the templates are normalised to unit flux at rest-frame wavelengths corresponding to  $\lambda_{\text{obs}} \geq 8000$  Å in the observer frame. We then apply the Small Magellanic Cloud (SMC) extinction law by [Prevot et al. \(1984\)](#) to both templates as shown in Fig. 2. The choice of an SMC-like extinction law stems from its capability of reproducing dust reddening of QSOs at all redshifts (e.g. [Richards et al. 2003](#); [Hopkins et al. 2004](#); [Bongiorno et al. 2007](#); [Gallerani et al. 2010](#); [Krawczyk et al. 2015](#)). Although the two

templates yield similar results, we adopt the xA QSOs template since it provides a more accurate description of the optical/UV behaviour of our sources. Even if the majority of our QSOs do not suffer from significant internal reddening, for a sizeable fraction of the sample ( $\sim 35\%$ ), the estimated  $E(B - V)$  is  $\geq 0.05$  and two sources, namely J1048+31 and J1207+15, show an  $E(B - V)$  of 0.13 and 0.2, respectively (see Tab. 4). The typical uncertainty on these reddening estimates is  $\sim 0.01$ . OM photometric data are corrected for the effects of both Galactic and internal dust extinction according to the same procedure.

Finally, the value of the monochromatic UV luminosity  $L_{2500\text{\AA}}$  for each QSO is obtained by linearly interpolating (or, if necessary, extrapolating) the OM data points at rest-frame 2500 Å. This is used jointly with the monochromatic X-ray luminosity at 2 keV estimated from the X-ray spectra (see Sect. 3.1) to calculate  $\alpha_{\text{ox}}$  as:

$$\alpha_{\text{ox}} = \log \left[ \frac{L_{\nu}(2 \text{ keV})}{L_{\nu}(2500 \text{ \AA})} \right] \bigg/ \log \left[ \frac{\nu(2 \text{ keV})}{\nu(2500 \text{ \AA})} \right] \\ \approx 0.384 \log \left[ \frac{L_{\nu}(2 \text{ keV})}{L_{\nu}(2500 \text{ \AA})} \right]. \quad (1)$$

We find that in our high- $\lambda_{\text{Edd}}$  AGN sample the bulk of the  $\alpha_{\text{ox}}$  values is around  $-1.8$ , with a minimum value of approximately  $-2.3$ .

## 4. Results

### 4.1. X-ray continuum slope

In Sect. 2 we mentioned that our AGN have been selected to span a narrow interval of  $\lambda_{\text{Edd}}$ , with  $0.9 \leq \lambda_{\text{Edd}} \leq 1.2$ . This

<sup>4</sup> <http://skyserver.sdss.org/dr16/en/home.aspx>.

<sup>5</sup> <https://irsa.ipac.caltech.edu/applications/DUST/>.

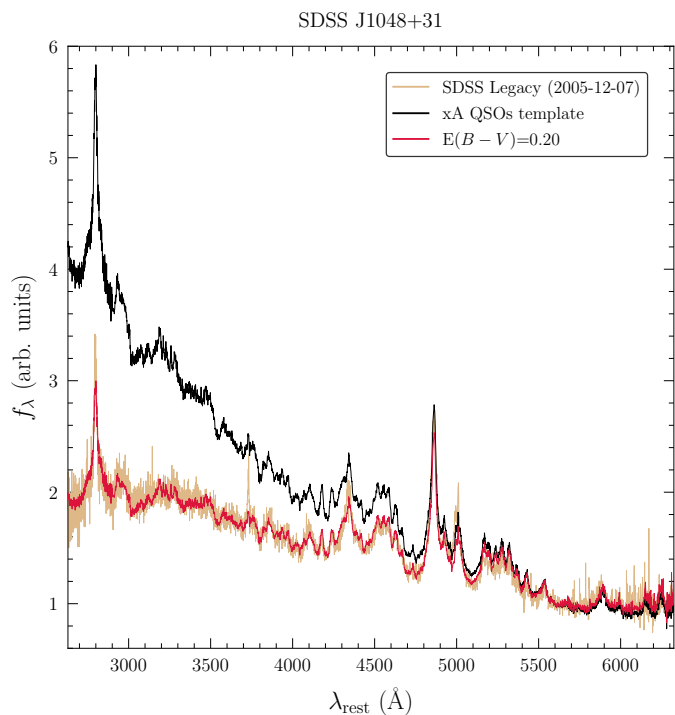


**Fig. 2:** SDSS spectrum of J1048+31 at  $z = 0.452$  (in gold) compared to the composite template of xA QSOs created by Marziani et al. (*in prep.*). The template (in black) is extinguished according to the SMC extinction law by Prevot et al. (1984), with progressively increasing values of  $E(B - V)$ . The value of  $E(B - V)$  for which the reddened template (in red) matches with the observed SDSS spectrum, corresponds to our estimate of the internal reddening of the source. J1048+31 has the largest  $E(B - V)$  among our sources, i.e.  $E(B - V) = 0.2$

enables us to investigate the properties of these sources on a statistical basis and reduce the effect of washing out possible correlations due to considering sources in a wide range of  $\lambda_{\text{Edd}}$ . Nonetheless, Fig. 3 shows that the continuum slope of the high- $\lambda_{\text{Edd}}$  AGN exhibits quite a large scatter. The values of  $\Gamma$  found by our analysis indeed span from  $\sim 1.3$  to  $\sim 2.5$ , with a non-negligible number of sources having quite flat photon indices  $\Gamma \lesssim 1.6$ . Furthermore, the flat X-ray continuum does not seem to be exclusively associated with an X-ray weak state (see Sect. 4.2). Indeed, out of the four  $\Gamma \leq 1.6$  sources in Fig. 3, only two are also X-ray weak (namely, J1103+41 and J1127+64). Interestingly, the presence of a consistent fraction ( $\sim 30\%$ ) of high- $\lambda_{\text{Edd}}$  AGN with flat  $\Gamma$  in our sample is at odds with the expectations based on the popular  $\Gamma - \lambda_{\text{Edd}}$  relations reported in previous works (e.g. Shemmer et al. 2008; Risaliti et al. 2009; Brightman et al. 2013), which predict steeper  $\Gamma$  of  $\sim 2 - 2.3$  for AGN with  $\lambda_{\text{Edd}} \sim 1$ .

However, Trakhtenbrot et al. (2017) found that the above relation between  $\Gamma$  and  $\lambda_{\text{Edd}}$  could be less steep than expected. They considered 228 hard X-ray selected AGN from the *Swift*/BAT AGN spectroscopic survey (BASS), with redshift  $0.01 < z < 0.5$ ,  $0.001 \lesssim \lambda_{\text{Edd}} \lesssim 1$ , and  $6 \lesssim \log(M_{\text{BH}}/M_{\odot}) \lesssim 9.5$ , which benefit from high-quality and broadband X-ray spectral coverage. For their BASS sample, Trakhtenbrot et al. (2017) found a statistically significant, albeit very weak correlation between  $\Gamma$  and  $\lambda_{\text{Edd}}$ . To complete the picture, in a recent paper, Liu et al. (2021) analysed a sample of 47 local, radio-quiet AGN with an accurate  $M_{\text{BH}}$  measurement from reverberation mapping, which includes both sub- and super-Eddington (i.e.  $\lambda_{\text{Edd}} \geq 0.3$ )

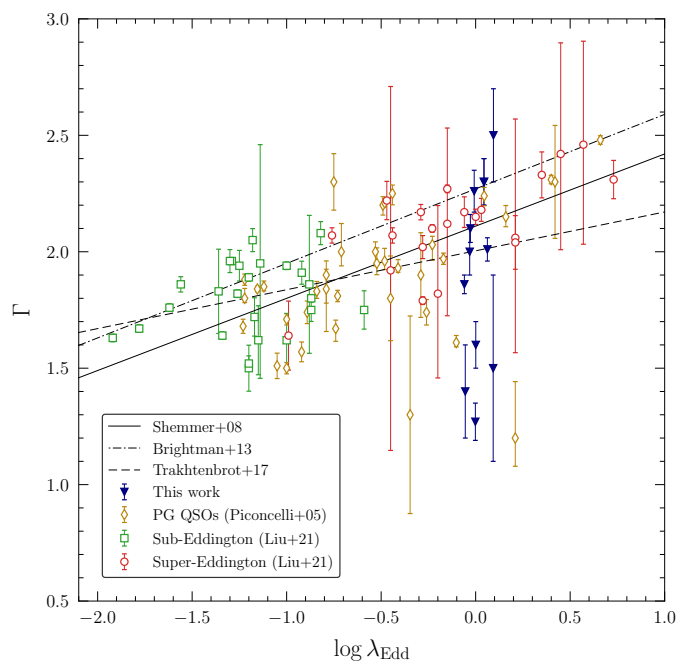


**Fig. 3:**  $\Gamma$  vs  $\log \lambda_{\text{Edd}}$  for the high- $\lambda_{\text{Edd}}$  QSOs in our sample (blue triangles). Two sources, J0300–08 and J1245+33, are excluded since their  $\Gamma$  were unconstrained by *XMM-Newton* data. J0940+46 and J1127+11 are described by the same point, since they share the same values of  $\Gamma$  and  $\lambda_{\text{Edd}}$ . Black solid, dashed and dash-dotted lines indicate the expected relation from other studies. Gold diamonds represent the sample of PG QSOs from Piconcelli et al. (2005). Green squares and red circles indicate the sub- and super-Eddington (i.e.  $\lambda_{\text{Edd}} \geq 0.3$ ) AGN from Liu et al. (2021), respectively.

sources. They found a significant correlation between  $\Gamma$  and  $\lambda_{\text{Edd}}$  for the full sample, as well as for the super-Eddington subsample, with a slope of  $\sim 0.3$ , consistent with that derived by, e.g. Shemmer et al. (2008) and Brightman et al. (2013). However, it is worth noting that for their study Liu et al. (2021) did only consider spectra during high-flux states, in case of AGN with multiple X-ray observations, which may lead to a possible bias in estimating the slope of the best-fit relation for high- $\lambda_{\text{Edd}}$  sources, given the trend of steeper-when-brighter typically observed in type-1 AGN (e.g. Leighly et al. 1996; Nandra et al. 1997; Gibson & Brandt 2012; Gliozzi et al. 2017; Serafinelli et al. 2017).

#### 4.2. X-ray weakness

Another relevant aspect emerging from the X-ray analysis of our high- $\lambda_{\text{Edd}}$  AGN sample is shown in Fig. 4. Our sources (blue triangles) are compared with the  $k_{\text{bol,X}}$  vs  $\log \lambda_{\text{Edd}}$  distribution of the XMM-COSMOS sample of type-1 AGN from Lusso et al. (2010), and the  $k_{\text{bol,X}} - \log \lambda_{\text{Edd}}$  best-fit relation from Duras et al. (2020), which holds for both absorbed (type-2) and unabsorbed (type-1) AGN, is also reported. The bulk of our sources is on average slightly above the range  $\sim 10 - 100$  expected for their  $\log \lambda_{\text{Edd}}$ . Furthermore there are four high- $\lambda_{\text{Edd}}$  AGN ( $\sim 30\%$  of the sample) exhibiting  $k_{\text{bol,X}}$  values significantly larger than expected and spanning a range between  $\sim 600 - 5000$ , i.e. larger than the maximum  $k_{\text{bol,X}}$  of  $\sim 400$  predicted by the Duras et al. (2020) relation for the most highly-accreting AGN. These high- $k_{\text{bol,X}}$  (hence X-ray weak) QSOs are J1103+41, J1127+64, J1245+33 and J0300–08, with the latter showing a  $k_{\text{bol,X}}$  of a few thousands. The left panel of Fig. 5 shows the distribution

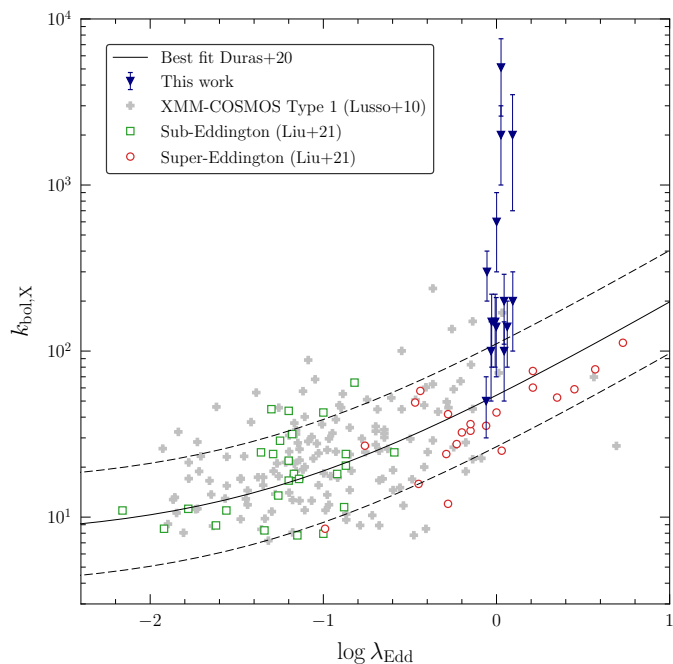


**Fig. 4:**  $k_{\text{bol},X}$  vs  $\log \lambda_{\text{Edd}}$  for the high- $\lambda_{\text{Edd}}$  AGN in our sample (blue triangles) compared to the XMM-COSMOS type-1 AGN (light grey crosses) of Lusso et al. (2010) with available measurement of Eddington ratio. Black solid line refers to the best-fit relation from Duras et al. (2020). Black dashed lines describe the  $1\sigma$  spread of the above relation. Green squares and red circles indicate the sub- and super-Eddington AGN from Liu et al. (2021), respectively.

of the high- $\lambda_{\text{Edd}}$  AGN in terms of the  $\alpha_{\text{ox}}$  parameter and the monochromatic optical/UV luminosity at  $2500 \text{ \AA}$ ,  $\log L_{\text{UV}}$ , and provides an additional piece of evidence to support this scenario. The same four QSOs are clearly offset from the  $\alpha_{\text{ox}}$  vs  $\log L_{\text{UV}}$  relation found for large AGN samples (e.g. Just et al. 2007; Lusso et al. 2010; Vagnetti et al. 2010; Martocchia et al. 2017), falling in the region of the plane defined by  $\Delta\alpha_{\text{ox}} \leq -0.3$ , where  $\Delta\alpha_{\text{ox}}$  represents the difference between the observed value of  $\alpha_{\text{ox}}$  and the expected value from the Lusso et al. (2010) relation. In their recent work, Pu et al. (2020) argued that those sources with  $\Delta\alpha_{\text{ox}} \leq -0.3$  can be reasonably classified as X-ray weak AGN (e.g. Brandt et al. 2000; Miniutti et al. 2009), given that such a  $\Delta\alpha_{\text{ox}}$  implies a  $L_{2-10\text{keV}}$  weaker by a factor of  $f_{\text{weak}} = 10^{-\Delta\alpha_{\text{ox}}/0.3838} \geq 6$  than the bulk of the AGN population at a similar  $\log L_{\text{UV}}$ . Specifically, the X-ray weakness factors  $f_{\text{weak}}$  measured for J1103+41, J1127+64, J1245+33 and J0300-08 span from  $\sim 11$  to  $\sim 75$ , with  $\Delta\alpha_{\text{ox}}$  comprised between  $-0.7$  and  $-0.4$ . It is worth noting that the fraction of QSOs with  $f_{\text{weak}} \geq 6$  in our sample is  $29_{-14}^{+22}\%$  (with errors estimated according to Gehrels 1986), which is much larger (and inconsistent at the  $\sim 99\%$  confidence level) than that derived by Pu et al. (2020) for a sample of 1825 type-1 QSOs from SDSS, i.e.  $5.8 \pm 0.7\%$ . The  $\alpha_{\text{ox}} - \log \lambda_{\text{Edd}}$  distribution of our fourteen high- $\lambda_{\text{Edd}}$  AGN, the XMM-COSMOS type-1 AGN of Lusso et al. (2010), the sub- and super-Eddington AGN of Liu et al. (2021) and the thirteen hyper-luminous WISSH QSOs of Zappacosta et al. (2020), divided in different regimes of bolometric luminosity, is shown in the right panel of Fig. 5. A large scatter around the best-fit relation from Lusso et al. (2010) is clearly visible in Fig. 5, and is probably reflecting the difficulty to derive a tight  $\alpha_{\text{ox}} - \log \lambda_{\text{Edd}}$  relation for large samples of sources with different bolometric luminosities.

Finally, Fig. 6 shows the distribution of the fourteen highly-accreting QSOs in the plane  $k_{\text{bol},X} - \alpha_{\text{ox}}$ , along with the relation derived for the COSMOS type-1 AGN that exhibit  $k_{\text{bol},X}$  in the range  $\approx 10 - 100$ . Typical local AGN in the sample of Liu et al. (2021) are also presented for comparison. The four X-ray weak high- $\lambda_{\text{Edd}}$  AGN are also located near the  $k_{\text{bol},X} - \alpha_{\text{ox}}$  relation in Lusso et al. (2010), being these two quantities closely related with each other, both of them indicating the relative strength between the X-ray emission produced in the corona and the UV emission from the accretion disc. Furthermore, it appears that the addition of a large number of X-ray weak sources might be useful to establish the exact  $k_{\text{bol},X} - \alpha_{\text{ox}}$  relation in a broad range of  $\alpha_{\text{ox}}$ , with the latter serving as a proxy for  $\log L_{\text{bol}}$ .

## 5. Discussion

### 5.1. Properties of the X-ray continuum and X-ray weakness

The 14 high- $\lambda_{\text{Edd}}$  AGN analysed in this paper are drawn from the larger MS14 sample of intermediate-redshift, highly-accreting quasars, which exhibit remarkably homogeneous optical properties (e.g. extremely strong Fe II emission, weak [O III] emission,  $\text{FWHM}(\text{H}\beta) < 4000 \text{ km s}^{-1}$ ). Furthermore, our sample has a narrow distribution in both redshift ( $\sigma_z \sim 0.1$ ) centred at  $z \sim 0.57$ , and Eddington ratio ( $\sigma_{\lambda_{\text{Edd}}} \sim 0.1$ ) centred at  $\lambda_{\text{Edd}} \sim 1.1$ , while luminosities and SMBH masses are clustered around  $\log(L_{\text{bol}}/\text{erg s}^{-1}) \approx 46.5$  and  $\log(M_{\text{BH}}/M_{\odot}) \approx 8.3$ , respectively (see Tab. 1). The main result emerging from our analysis is that, despite the homogeneous optical and SMBH accretion properties, the X-ray properties of these xA quasars appear to be quite heterogeneous. This, in turn, indicates that the structure and efficiency of the X-ray corona and innermost accretion flow in these AGN cannot be considered a uniform and distinctive feature for reaching a maximised radiative output per unit mass. In this sense, the scatter of the primary continuum slope measured for our highly-accreting quasars as a function of the logarithm of  $\lambda_{\text{Edd}}$  (Fig. 3) suggests caution in the use of  $\Gamma$  for providing a reliable estimate of the SMBH mass based on the X-ray spectrum. Indeed, at these high-Eddington ratios this may be telling us something about the structure of the disc/corona complex, possibly indicating a (time-variable?) redistribution of disc accretion power dissipated in the corona, such as a variation in the inner truncation radius of the accretion disc or the geometry of the disc/corona complex (e.g. Kubota & Done 2018). This, in turn, would affect the slope of the hard X-ray emission. In particular, a larger number of sources with  $M_{\text{BH}}$  at the high-end of the mass distribution (i.e.  $\geq 10^9 M_{\odot}$ ) and a well-constrained hard X-ray photon index is needed to evaluate the presence of possible biases due to a dependence of  $\Gamma$  on  $M_{\text{BH}}$  (e.g. Martocchia et al. 2017).

Another piece of evidence supporting a large variety of the X-ray properties of our high- $\lambda_{\text{Edd}}$  quasars comes from the wide distributions of  $k_{\text{bol},X} - \log \lambda_{\text{Edd}}$  and  $\alpha_{\text{ox}} - \log L_{\text{UV}}$  reported in Fig. 4 and 5. In particular, four sources exhibit large values of  $k_{\text{bol},X}$  and small  $\Delta\alpha_{\text{ox}}$ , and they can be classified as X-ray weak quasars. For these sources, we measure an X-ray emission about a factor of  $\sim 10 - 80$  fainter than the bulk of the AGN population at similar UV luminosities. Bearing in mind the uncertainties due to the limited number of sources, the fraction of QSOs with  $f_{\text{weak}} \geq 6$  in our sample is  $29_{-14}^{+22}\%$ , which is much larger than that derived for the AGN general population (e.g. Pu et al. 2020), suggesting a possible change in the properties of the accretion disc-corona system in some objects radiating close (or above) to the Eddington limit, possibly related to the increas-

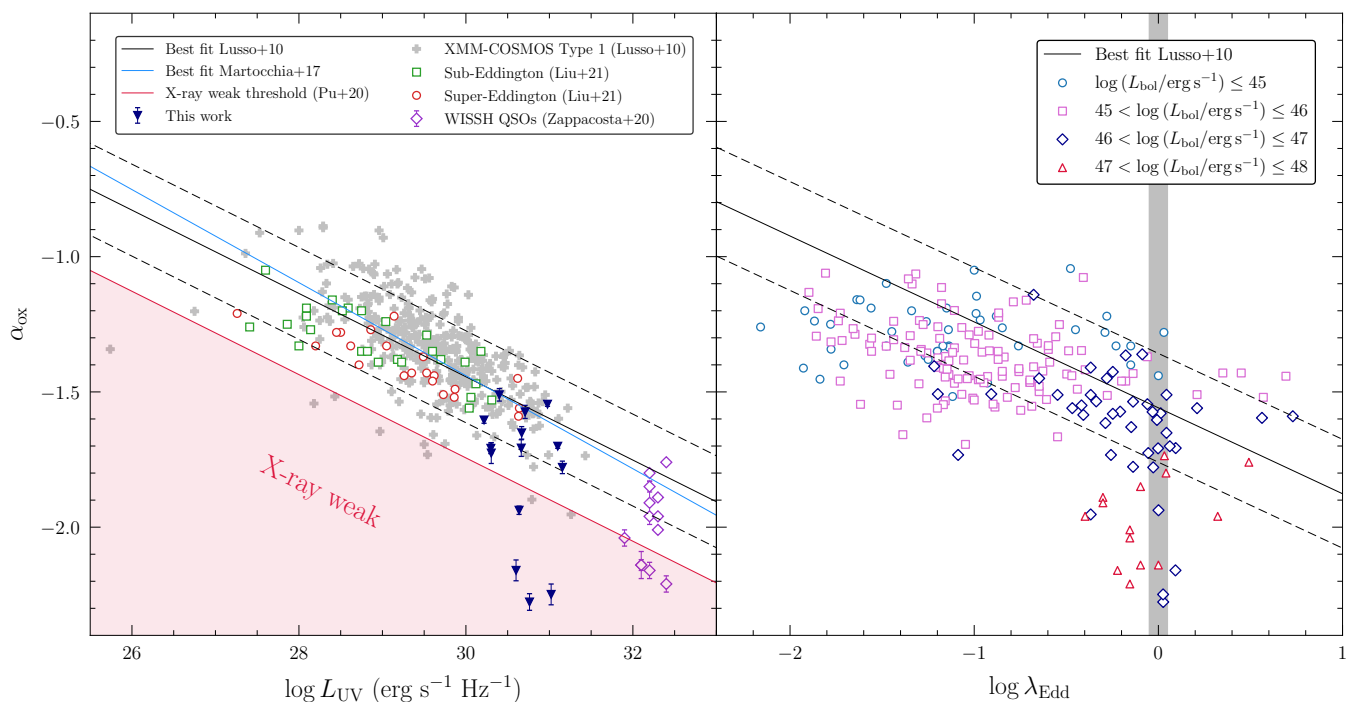


**Fig. 5:** *Left panel:*  $\alpha_{\text{ox}}$  vs  $\log L_{\text{UV}}$  for our high- $\lambda_{\text{Edd}}$  AGN (blue triangles) compared to the XMM-COSMOS type-1 AGN (light grey crosses) of Lusso et al. (2010). Black solid line is the best-fit relation from the same authors. Black dashed lines describe the  $1\sigma$  spread of the above relation. Blue solid line is the best-fit relation obtained from Martocchia et al. (2017). Green squares and red circles indicate the sub- and super-Eddington AGN from Liu et al. (2021), respectively. Purple diamonds are the 13 WISSH QSOs from Zappacosta et al. (2020). Red solid line marks the reference value for X-ray weakness, i.e.  $\Delta\alpha_{\text{ox}} \leq -0.3$  (Pu et al. 2020). *Right panel:* distribution of the same sources described in the adjacent panel, divided in two regimes of bolometric luminosity, in the  $\alpha_{\text{ox}} - \log \lambda_{\text{Edd}}$  plane. For the XMM-COSMOS AGN sample, only those sources with available measurement of  $\lambda_{\text{Edd}}$  are included. Black solid line indicates the best-fit relation from Lusso et al. (2010). Black dashed lines describe the  $1\sigma$  spread of the above relation. The shaded interval at  $\log \lambda_{\text{Edd}} \sim 0$  is included to highlight that AGN with very similar values of  $\lambda_{\text{Edd}}$  can show a widespread distribution in  $\alpha_{\text{ox}}$  due to their different  $L_{\text{bol}}$ .

ing importance of radiation pressure in shaping the efficiency of the accretion process (e.g. Proga & Kallman 2004; Sądowski & Narayan 2016; Zappacosta et al. 2020; Nomura et al. 2020). We note that X-ray weakness in highly-accreting quasars is often attributed to absorption. This has typically been the case for BAL quasars (Gallagher et al. 2002; Piconcelli et al. 2005; but see also Morabito et al. 2014 and Teng et al. 2014) and weak emission-line quasars (WLQs; e.g. Luo et al. 2015; Ni et al. 2018), for which the presence of a nuclear shielding gas component with a large covering factor has been proposed to explain the weak broad emission lines and wind acceleration without over-ionisation (e.g. Wu et al. 2011). In the case of high- $\lambda_{\text{Edd}}$  AGN, this shielding gas may be identified with an optically and geometrically thick accretion disc (Luo et al. 2015), or with a failed wind resulting from stalling of line-driven disc winds (e.g. Proga & Kallman 2004; Proga 2005; Nomura et al. 2020). In any case, the shielding gas should also be responsible for the X-ray absorption along our line of sight to the nucleus. Both BAL quasars and WLQs are indeed characterised by hard X-ray spectra, when the broadband continuum is modelled with a single power law. Indeed, on average, the resulting effective photon index is usually  $\langle\Gamma_{\text{eff}}\rangle \sim 1.2$ . Pu et al. (2020), for instance, indicated  $\Gamma_{\text{eff}} = 1.26$  as the threshold below which a quasar is potentially obscured by cold absorption. However, by modelling the 0.3 – 10 keV X-ray continuum with a power law, we find none of our four high- $\lambda_{\text{Edd}}$  X-ray weak sources to have flat photon indices compatible with those typical of WLQs and other absorbed quasars. Indeed, they show very steep  $\Gamma_{\text{eff}} \sim 2.2 - 3$ , suggesting that intervening cold obscuration is not the likely cause of their

X-ray weakness, which may therefore be an intrinsic property of these AGN. Nonetheless, we cannot rule out the presence of a highly-ionised gas cloud with a large  $N_{\text{H}}$  and small covering factor along our line of sight which may scatter off a large amount of photons, causing a decrease of the X-ray flux without altering the spectral shape. However, this *ad hoc* scenario is difficult to test directly and seems quite unlikely to apply to all the four X-ray weak QSOs in our sample. In addition, Miniutti et al. (2012) proposed a couple of alternative scenarios for the intrinsic X-ray weakness of the  $z \sim 0.4$ , high- $\lambda_{\text{Edd}}$  quasar PHL 1092, which is one of the most extreme X-ray weak quasars with no BAL and an almost constant flux in the UV. In the former scenario, the size of the X-ray corona changes as a function of the X-ray flux, and a very compact X-ray corona further shrinks down to the innermost stable circular orbit around the SMBH during X-ray weak states. In the second scenario, the corona is located within few gravitational radii from the SMBH at all flux levels, and light-bending effects give rise to a disc reflection-dominated X-ray spectrum in extreme low-flux states. However, this hypothesis can be tested only by analysing additional, deeper X-ray observations (preferably including data at  $> 10$  keV) to reveal typical relativistic reflection spectral features. Similarly, light-bending effects have also been invoked by Ni et al. (2020) as a viable explanation to justify the extreme X-ray variability of the  $z = 1.935$ , WLQ SDSS J153913.47+395423.4. This source was found to be in an X-ray weak state, before its flux raised by a factor of  $\sim 20$ , approximately six years after its first observation (corresponding to  $\sim 2$  years in the QSO rest frame). Alternatively, the authors also suggested that the X-ray weakness could

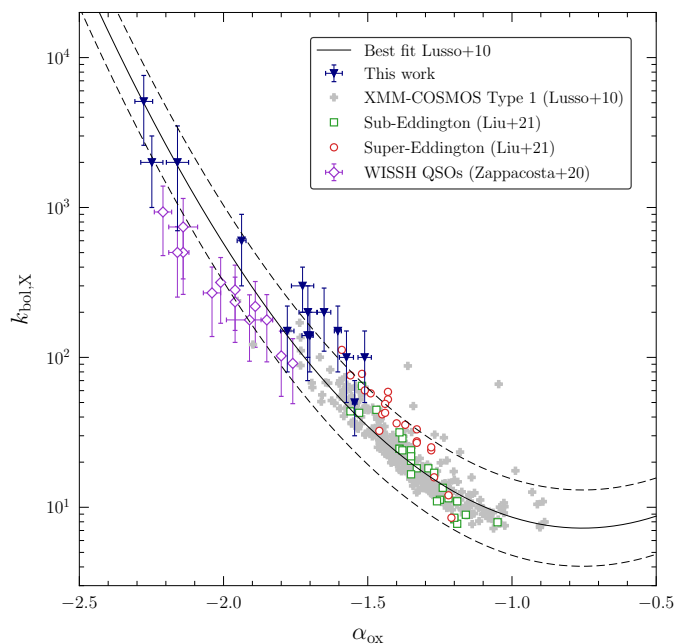


**Fig. 6:**  $k_{\text{bol},X}$  vs  $\alpha_{\text{ox}}$  for the high- $\lambda_{\text{Edd}}$  AGN in our sample (blue triangles) compared to the XMM-COSMOS type-1 AGN (light grey crosses) of Lusso et al. (2010). Black solid line refers to their best-fit relation, with the black dashed lines describing its  $1\sigma$  spread. Green squares and red circles indicate the sub- and super-Eddington AGN from Liu et al. (2021), respectively. Purple diamonds are the hyper-luminous WISSH QSOs from Zappacosta et al. (2020).

be caused by nuclear shielding, probably due to the inner thick disc, which may intercept the line of sight to the central source.

High- $\lambda_{\text{Edd}}$  AGN are also likely to accelerate powerful outflows, which can provide an additional effect contributing to weaken the X-ray emission. Laurenti et al. (2021) analysed the UFO in the NLSy1 galaxy PG 1448+273 with  $\lambda_{\text{Edd}} \sim 0.75$ . They found that this source underwent large variations of  $\alpha_{\text{ox}}$ , with a maximum offset of  $\Delta\alpha_{\text{ox}} = -0.7$ , after the UFO was detected. As a result, PG 1448+263 was characterised by a remarkable X-ray weakness for some months, before the flux finally returned to the same level as prior to the UFO detection. In this case, the authors suggested that such a powerful disc wind could be responsible of the observed X-ray weakness, by removing a large amount of the infalling material in the innermost part of the accretion disc and, thus, reducing the flux of seed photons towards the corona.

In addition, Zappacosta et al. (2020) recently reported a relation between  $L_{2-10}$  and the velocity shift  $v_{\text{CIV}}$  of the C IV emission line profile over  $\sim 1.5$  dex in  $L_{2-10\text{keV}}$  for a sample of thirteen very luminous quasars at  $z > 2$ , with  $\lambda_{\text{Edd}} \sim 0.5 - 3$  estimated from H $\beta$ -based  $M_{\text{BH}}$ . These C IV shifts are interpreted in terms of winds produced at accretion-disc scale, and the fastest winds appear to be associated with the lowest hard X-ray luminosities and steepest  $\alpha_{\text{ox}}$  values. Interestingly, Proga (2005) suggests that in case of highly-accreting AGN, failed winds, which are inevitably produced along with UV line-driven winds, may affect the density of the X-ray corona and weaken its inverse Compton X-ray emission.

Zappacosta et al. (2020) found that X-ray weak sources (i.e. those with  $\Delta\alpha_{\text{ox}} \leq -0.3$ ) represent a fraction of  $\sim 40\%$  of their sample and all exhibit  $v_{\text{CIV}} \geq 5000$  km s $^{-1}$ . Nardini et al. (2019) have recently analysed the XMM spectra of a sample of 30 intrinsically blue, non-BAL,  $L_{\text{bol}} \gtrsim 10^{47}$  erg s $^{-1}$  quasars at  $z \sim 3 - 3.3$  which are likely to shine at  $\lambda_{\text{Edd}} \sim 1$  (see also Lusso

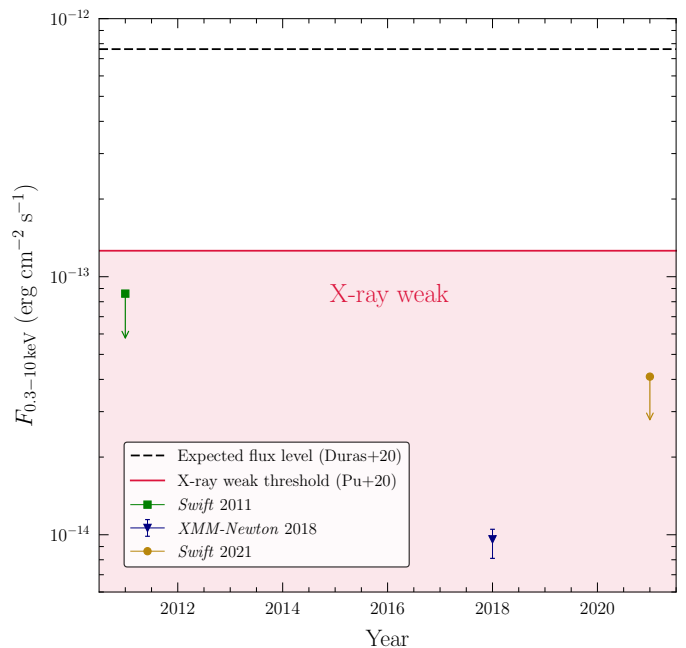


**Fig. 7:** Light curve of J0300–08 in terms of the broadband  $E = 0.3 - 10$  keV flux. Black dashed line represents the flux level of  $F_{0.3-10\text{keV}} = 7.6 \times 10^{-13}$  erg cm $^{-2}$  s $^{-1}$  expected from its bolometric luminosity, once the  $k_{\text{bol},X} - \log L_{\text{bol}}$  relation from Duras et al. (2020) is assumed. Red solid line indicates the flux reference value for X-ray weakness corresponding to  $\Delta\alpha_{\text{ox}} \leq -0.3$  (Pu et al. 2020). The  $3\sigma$  upper limits from the *Swift* observations of 2011 and 2021 are shown in green and gold, respectively. The flux from the 2018 *XMM-Newton* observation analysed in this work is marked in blue.

et al. 2021). They reported a fraction of  $\sim 25\%$  of X-ray weak sources, according to a  $-0.4 < \Delta\alpha_{\text{ox}} < -0.2$ . Interestingly, our finding of a similar fraction of X-ray weak sources in our sample of  $z \sim 0.6$ ,  $L_{\text{bol}} \sim 10^{46}$  erg s $^{-1}$ , optically-selected quasars therefore suggests that (i) a high frequency of intrinsically X-ray weak sources is not a distinctive feature of the population of ultra-luminous, high- $z$  quasars and (ii) a high- $\lambda_{\text{Edd}}$  ratio may imply favourable accretion disc conditions for enhancing the probability of catching an AGN in an X-ray weak state.

Finally, we were recently awarded time on the *Neil Gehrels Swift* Observatory (Gehrels et al. 2004, hereinafter *Swift*) for monitoring the X-ray emission of the four X-ray weak sources discovered by the *XMM-Newton* observations presented here and tracking down possible rises of their X-ray emission (PI: E. Piconcelli). The first observed source is J0300–08, which was targeted by *Swift* for 16 ks on March 2021. The source was not detected, with a  $3\sigma$  upper-limit on the 0.3 – 10 keV flux of  $4.1 \times 10^{-14}$  erg cm $^{-2}$  s $^{-1}$ , indicating that this quasar still exhibits a weak X-ray emission. Fig. 7 shows this value along with the fluxes derived from the 2018 *XMM-Newton* observation and from an additional *Swift* 6 ks archival observation performed in 2011, for which we derive an upper-limit of  $8.6 \times 10^{-14}$  erg cm $^{-2}$  s $^{-1}$ . According to the  $k_{\text{bol},X} - \log L_{\text{bol}}$  best-fit relation from Duras et al. (2020), from the  $\log L_{\text{bol}}$  listed in Tab. 1 for J0300–08 we would expect a flux of around  $F_{0.3-10\text{keV}} \sim 8 \times 10^{-13}$  erg cm $^{-2}$  s $^{-1}$ . All the measured X-ray fluxes are well below the level expected for the bulk of type-1 AGN with comparable  $\log L_{\text{bol}}$ , as shown in Fig. 7. This may indicate that J0300–08 has likely been in a predominantly low-flux state during the past decade, suggesting that the X-ray weakness regime may persist over a timescale of several years.

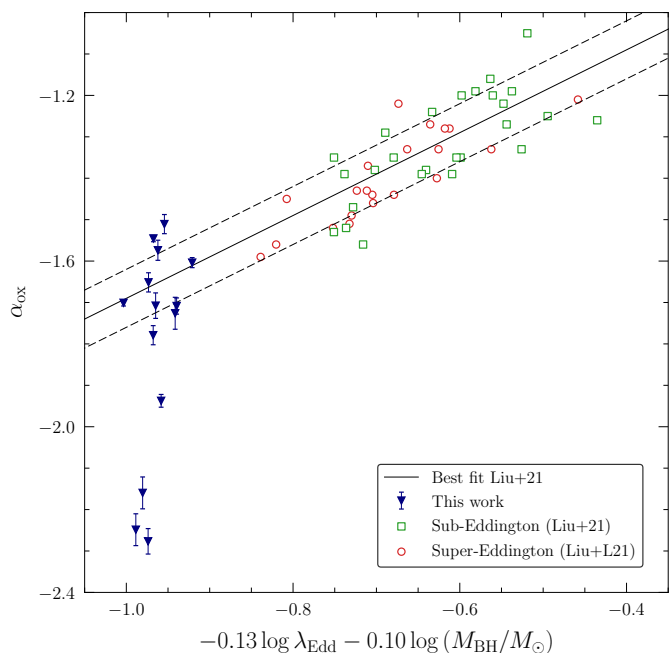


**Fig. 8:**  $\alpha_{\text{ox}} - \lambda_{\text{Edd}} - M_{\text{BH}}$  plane introduced by Liu et al. (2021). Green squares and red circles indicate their sub- and super-Eddington AGN, respectively. Black solid and dashed lines describe the best-fit relation and its spread as indicated by the same authors, respectively. We extend their relation towards higher accretion rates and black hole masses by including our high- $\lambda_{\text{Edd}}$  AGN (blue triangles).

## 5.2. Relations involving $\lambda_{\text{Edd}}$

The results presented in Sect. 4 highlight the importance of enlarging the number of high- $\lambda_{\text{Edd}}$  quasars with dedicated X-ray observations. This would enable new opportunities to investigate the high- $\lambda_{\text{Edd}}$  phenomenon at large and extend the dynamical range for any possible correlation involving X-ray derived parameters and the Eddington ratio. Specifically, Fig. 4 shows that the relation between  $k_{\text{bol,X}} - \log \lambda_{\text{Edd}}$  by Duras et al. (2020) seems to provide a fair description of the correlation for the bulk of the high- $\lambda_{\text{Edd}}$  AGN population, i.e. for both small- and large- $M_{\text{BH}}$  sources, except for the X-ray weak sources that deviate considerably from the best-fit relation. Conversely, the large scatter in the right panel of Fig. 5 indicates that only additional investigations involving a large number of high- $\lambda_{\text{Edd}}$  AGN at different luminosity regimes may deepen our understanding of the relation between  $\alpha_{\text{ox}}$  and  $\log \lambda_{\text{Edd}}$ . In particular, as shown in the same figure, sources with very similar values of  $\log \lambda_{\text{Edd}}$  can exhibit a widespread distribution of  $\alpha_{\text{ox}}$  values according to their  $L_{\text{bol}}$  ( $\approx L_{\text{UV}}$  in case of type-1 AGN). This suggests that the presence of a large scatter observed in the  $\alpha_{\text{ox}} - \log \lambda_{\text{Edd}}$  plane is intrinsic, and the accurate description of this relation for the whole AGN population should take into account this dependence on  $L_{\text{bol}}$ . This may also explain the opposite conclusions on the existence of a significant correlation between  $\alpha_{\text{ox}} - \log \lambda_{\text{Edd}}$  reported by different studies so far (e.g. Vasudevan & Fabian 2007; Shemer et al. 2008; Lusso et al. 2010; Chiaraluce et al. 2018).

Furthermore, Liu et al. (2021) have recently proposed the possible existence of a more complex scenario for the relation between  $\alpha_{\text{ox}}$  and  $\log \lambda_{\text{Edd}}$ , which also involves another fundamental parameter, i.e.  $M_{\text{BH}}$ . On the one hand they found that both sub- and super-Eddington AGN follow the same  $\alpha_{\text{ox}} - \log L_{\text{UV}}$  relation, which may indicate that the properties of the accretion disc-corona system do not show large differences as a function

of the accretion rate for the sources in their sample, which are all observed in a high-flux state. On the other hand, Liu et al. (2021) found that the anti-correlation between  $\alpha_{\text{ox}}$  and  $\log \lambda_{\text{Edd}}$  is more significant when the two subsamples of sub- and super-Eddington AGN are considered separately instead of the entire AGN sample. A similar behaviour is also observed for  $\alpha_{\text{ox}}$  as a function of  $\log (M_{\text{BH}}/M_{\odot})$ . Interestingly, by means of a partial correlation analysis, Liu et al. (2021) obtained a statistically significant non-linear relation between  $\alpha_{\text{ox}}$  and both  $\lambda_{\text{Edd}}$  and  $M_{\text{BH}}$ , in the form  $\alpha_{\text{ox}} = \beta \log \lambda_{\text{Edd}} + \gamma \log (M_{\text{BH}}/M_{\odot}) + \delta$ , with  $\beta \approx -0.13$ ,  $\gamma \approx -0.10$  and  $\delta \approx -0.69$ . This best fit is shown in Fig. 8 along with the data from the Liu et al. (2021) sub- and super-Eddington samples. The relation appears to hold once extended towards steeper  $\alpha_{\text{ox}}$  and larger  $M_{\text{BH}}$  by including our high- $\lambda_{\text{Edd}}$  quasars. Clearly, being based on sources observed in a high-flux state, the Liu et al. (2021) relation cannot describe the behaviour of the four X-ray weak sources in our sample. On the basis of their data Liu et al. (2021) were not able to determine whether this  $\alpha_{\text{ox}} - \lambda_{\text{Edd}} - M_{\text{BH}}$  relation represents the fundamental plane, or a secondary effect of the  $\alpha_{\text{ox}} - \log L_{\text{UV}}$  relation. Moreover,  $\alpha_{\text{ox}}$ ,  $\lambda_{\text{Edd}}$ , and  $M_{\text{BH}}$  are all intimately connected and cannot be considered as independent variables. This suggests to use caution when determining relations that involve these quantities. However, the investigation on the nature of the physical driver of these relations will certainly be a hotly-debated topic in the future.

Finally, it is worth noting that although most of our high- $\lambda_{\text{Edd}}$  QSOs are basically unobscured in the optical, five sources are characterised by an internal reddening  $E(B - V) \geq 0.05$ , and two of them having  $E(B - V) \geq 0.1$  (see Tab. 4). This is particularly intriguing since Krawczyk et al. (2015) analysed both the reddening and extinction of  $\sim 35000$  type-1 QSOs from the SDSS, with  $z \leq 5$  including both BAL and non-BAL quasars. They concluded that only 9% (35%) of the non-BAL (BAL) AGN has an  $E(B - V) \geq 0.05$ , and 3% (11%) has an  $E(B - V) \geq 0.1$ . This means that, independently of their classification as non-BAL or BAL QSOs, the five reddened, high- $\lambda_{\text{Edd}}$  AGN in our sample belong to the right-hand tail of the reddening distribution of type-1 AGN. For what concerns the X-ray appearance of these five sources, we do not find any trend with  $E(B - V)$ , as their main X-ray spectral properties are widely heterogeneous. Indeed, they show a power-law continuum with photon indices comprised between  $1.3 \leq \Gamma \leq 2.3$ , values of  $\alpha_{\text{ox}}$  between  $\sim -1.6$  and  $\sim -1.9$ , and the  $R_{\text{S/P}}$  parameter ranges from  $\sim 0.5$  to  $\sim 5.5$ . In addition, only one out of five reddened sources (namely J1103+41) can be classified as X-ray weak quasar, showing a  $k_{\text{bol,X}} = 600 \pm 300$ .

## 6. Summary and conclusion

In this study, we have investigated the X-ray and optical/UV properties of 14 high- $\lambda_{\text{Edd}}$ , radio-quiet quasars observed by *XMM-Newton* (see Sect. 2). These sources belong to the sample of intermediate-redshift, highly-accreting quasars presented in MS14, and are characterised by homogeneous spectral optical and SMBH (i.e.  $M_{\text{BH}}$  and  $\lambda_{\text{Edd}}$ ) properties. The main results can be summarised as follows:

1. Our high- $\lambda_{\text{Edd}}$  quasars exhibit significant differences in their X-ray properties. Specifically, we find a large scatter in the distribution of the continuum slope, with a non-negligible fraction of these AGN showing  $\Gamma \leq 1.6$  (see Fig. 3). Bearing in mind the limited number of sources analysed here, this result suggests that the X-ray properties of high- $\lambda_{\text{Edd}}$  AGN can be more heterogeneous than previously reported. In this

sense, the observed offsets from the  $\Gamma$  vs  $\lambda_{\text{Edd}}$  relations found in the past (e.g. Shemmer et al. 2008; Brightman et al. 2013; Huang et al. 2020) can be a manifestation of distinctive physical properties of the inner accretion disc–X-ray corona in these AGN.

2. We also find that  $\sim 30\%$  of the high- $\lambda_{\text{Edd}}$  sources considered in our study show an X-ray weakness factor  $f_{\text{weak}} > 10$  corresponding to  $\Delta\alpha_{\text{ox}}$  comprised between  $-0.7$  and  $-0.4$  (see Figs. 5 and 6). They can be therefore classified as X-ray weak quasars. The steep broad-band X-ray spectral shape (i.e.  $\Gamma_{\text{eff}} \geq 2.2$ ; see Sect. 5.1) seems to rule out absorption as the cause of their reduced X-ray emission, lending support to an intrinsic X-ray weakness. Interestingly, this fraction is similar to that reported by Nardini et al. (2019) and Zappacosta et al. (2020) who studied samples of very luminous ( $L_{\text{bol}} \gtrsim 10^{47}$  erg s $^{-1}$ ) quasars at  $z \sim 2 - 3$ , which are likely to shine at  $\lambda_{\text{Edd}} \gtrsim 1$ . This indicates that a high  $\lambda_{\text{Edd}}$  might be a key parameter for triggering a weak X-ray corona state. A systematic X-ray/UV study of large samples of  $\lambda_{\text{Edd}} \geq 1$  AGN would therefore be useful to shed light on the distinctive nuclear properties of sources undergoing an intrinsically X-ray weak phase. Furthermore, a recent *Swift* monitoring of J0300–08, one of the four X-ray weak QSOs in our sample, reveals that the source was still in a low-flux state in March 2021. Combining this measurement with the 2018 *XMM-Newton* and an archival 2011 *Swift* observation, it appears that J0300–08 has likely been going through a period of intrinsic X-ray weakness for nearly a decade (see Fig. 7).
3. The analysis of the optical spectra of the fourteen high- $\lambda_{\text{Edd}}$  quasars reveals that five sources have a reddening  $E(B - V) \geq 0.05$ . Such a fraction of reddened sources is higher than that typically measured for the non-BAL quasar population, and we do not report any apparent link with specific X-ray spectral and  $\Delta\alpha_{\text{ox}}$  properties. Spectroscopy in the UV band would be very useful to detect the possible presence of BAL features in these reddened, highly-accreting quasars at intermediate redshifts and shed light on their nature.

We note that, given the relatively bright 0.5–2 keV fluxes of the quasars in the present sample and the expected soft X-ray flux limits of the eROSITA surveys (eRASS:1, i.e. first full-sky data release:  $\approx 4.5 \times 10^{-14}$  erg cm $^{-2}$  s $^{-1}$ ; eRASS:8, final full-sky data release:  $\approx 1 \times 10^{-14}$  erg cm $^{-2}$  s $^{-1}$ ; Merloni et al. 2012), we can expect that  $\approx 70 - 80\%$  of our highly-accreting quasars will be detected by eROSITA. However, the paucity of X-ray photons provided by eROSITA in survey mode will strongly limit any detailed X-ray spectral analysis, thus calling for more sensitive pointed X-ray observations.

Finally, the results presented in this paper inspire the following lines of future investigation: (i) a monitoring of the X-ray flux of the high- $\lambda_{\text{Edd}}$  quasars analysed here, both X-ray “normal” and “weak” ones, over multiple timescales (i.e. months to years). This would allow us to get useful insights on the frequency and duration of the transitions between these two states; (ii) deep X-ray spectroscopy of the X-ray weak quasars is also desirable to provide unambiguous constraints on the spectral shape and the possible presence of some absorption along our line of sight to the nucleus.

*Acknowledgements.* We thank the anonymous referee for her/his useful comments. This work is based on observations obtained with *XMM-Newton*, an ESA science mission with instruments and contributions directly funded by ESA Member States and NASA. Part of this work is based on archival data, software and online services provided by the Space Science Data Center - ASI. This work has been partially supported by the ASI-INAF program I/004/11/4. ML

acknowledges financial support from the Ph.D. programme in Astronomy, Astrophysics and Space Science supported by MIUR (Ministero dell’Istruzione, dell’Università e della Ricerca). EP, LZ, FT, SB, AL and GV acknowledge financial support under ASI/INAF contract 2017-14-H.O. EP, SB, MB and GV acknowledge support from PRIN MIUR project “Black Hole winds and the Baryon Life Cycle of Galaxies: the stone-guest at the galaxy evolution supper”, contract #2017PH3WAT. AdO acknowledges financial support from the State Agency for Research of the Spanish MCIU through the project PID2019-106027GB-C41 and the “Center of Excellence Severo Ochoa” award to the Instituto de Astrofísica de Andalucía (SEV-2017-0709). RM acknowledges the financial support of INAF (Istituto Nazionale di Astrofisica), Osservatorio Astronomico di Roma, ASI (Agenzia Spaziale Italiana) under contract to INAF: ASI 2014-049-R.0 dedicated to SSDC. CR acknowledges support from the Fondecyt Iniciación grant 11190831.

## References

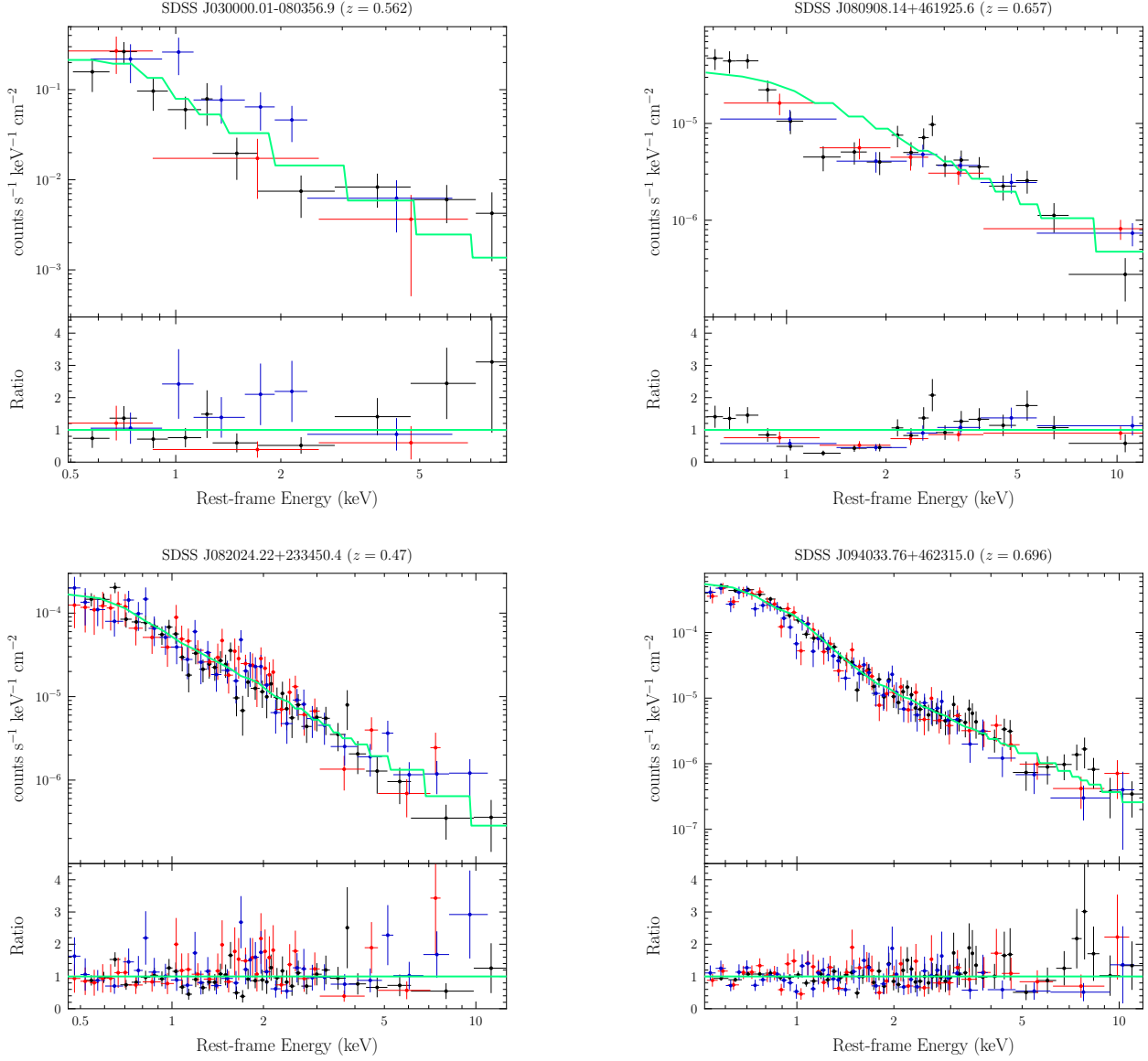
- Abramowicz, M. A., Czerny, B., Lasota, J. P., & Szuszkiewicz, E. 1988, *ApJ*, 332, 646
- Arnaud, K. A. 1996, in *Astronomical Society of the Pacific Conference Series*, Vol. 101, *Astronomical Data Analysis Software and Systems V*, ed. G. H. Jacoby & J. Barnes, 17
- Avni, Y. 1976, *ApJ*, 210, 642
- Bañados, E., Venemans, B. P., Decarli, R., et al. 2016, *ApJS*, 227, 11
- Baskin, A. & Laor, A. 2005, *MNRAS*, 356, 1029
- Bianchi, S., Guainazzi, M., Matt, G., Fonseca Bonilla, N., & Ponti, G. 2009, *A&A*, 495, 421
- Bischetti, M., Piconcelli, E., Feruglio, C., et al. 2019, *A&A*, 628, A118
- Bischetti, M., Piconcelli, E., Vietri, G., et al. 2017, *A&A*, 598, A122
- Bongiorno, A., Zamorani, G., Gavignaud, I., et al. 2007, *A&A*, 472, 443
- Brandt, W. N., Laor, A., & Wills, B. J. 2000, *ApJ*, 528, 637
- Brandt, W. N., Mathur, S., & Elvis, M. 1997, *MNRAS*, 285, L25
- Brightman, M., Silverman, J. D., Mainieri, V., et al. 2013, *MNRAS*, 433, 2485
- Cash, W. 1979, *ApJ*, 228, 939
- Castelló-Mor, N., Kaspi, S., Netzer, H., et al. 2017, *MNRAS*, 467, 1209
- Chen, L.-H. & Wang, J.-M. 2004, *ApJ*, 614, 101
- Chiaraluca, E., Vagnetti, F., Tombesi, F., & Paolillo, M. 2018, *A&A*, 619, A95
- Collin, S., Kawaguchi, T., Peterson, B. M., & Vestergaard, M. 2006, *A&A*, 456, 75
- Costantini, E., Gallo, L. C., Brandt, W. N., Fabian, A. C., & Boller, T. 2007, *MNRAS*, 378, 873
- Dou, L., Wang, T.-G., Ai, Y., et al. 2016, *ApJ*, 819, 167
- Duras, F., Bongiorno, A., Ricci, F., et al. 2020, *A&A*, 636, A73
- Fabian, A. C., Kara, E., Walton, D. J., et al. 2013, *MNRAS*, 429, 2917
- Fanali, R., Caccianiga, A., Severgnini, P., et al. 2013, *MNRAS*, 433, 648
- Ferrarese, L. & Merritt, D. 2000, *ApJ*, 539, L9
- Fiore, F., Feruglio, C., Shankar, F., et al. 2017, *A&A*, 601, A143
- Fitzpatrick, E. L. 1999, *PASP*, 111, 63
- Fukumura, K., Hendry, D., Clark, P., Tombesi, F., & Takahashi, M. 2016, *ApJ*, 827, 31
- Gallagher, S. C., Brandt, W. N., Chartas, G., & Garmire, G. P. 2002, *ApJ*, 567, 37
- Gallerani, S., Maiolino, R., Juarez, Y., et al. 2010, *A&A*, 523, A85
- Gallo, L. C. 2006, *MNRAS*, 368, 479
- Gehrels, N. 1986, *ApJ*, 303, 336
- Gehrels, N., Chincarini, G., Giommi, P., et al. 2004, *ApJ*, 611, 1005
- Gibson, R. R. & Brandt, W. N. 2012, *ApJ*, 746, 54
- Glozzi, M., Papadakis, I. E., Grupe, D., Brinkmann, W. P., & Räth, C. 2017, *MNRAS*, 464, 3955
- Glozzi, M. & Williams, J. K. 2020, *MNRAS*, 491, 532
- HI4PI Collaboration, Ben Bekhti, N., Flöer, L., et al. 2016, *A&A*, 594, A116
- Hopkins, P. F. & Elvis, M. 2010, *MNRAS*, 401, 7
- Hopkins, P. F., Strauss, M. A., Hall, P. B., et al. 2004, *AJ*, 128, 1112
- Huang, J., Luo, B., Du, P., et al. 2020, *ApJ*, 895, 114
- Jansen, F., Lumb, D., Altieri, B., et al. 2001, *A&A*, 365, L1
- Jin, C., Done, C., Middleton, M., & Ward, M. 2013, *MNRAS*, 436, 3173
- Just, D. W., Brandt, W. N., Shemmer, O., et al. 2007, *ApJ*, 665, 1004
- King, A. & Pounds, K. 2015, *ARA&A*, 53, 115
- Krawczyk, C. M., Richards, G. T., Gallagher, S. C., et al. 2015, *AJ*, 149, 203
- Kubota, A. & Done, C. 2018, *MNRAS*, 480, 1247
- Laurenti, M., Luminari, A., Tombesi, F., et al. 2021, *A&A*, 645, A118
- Leighly, K. M., Mushotzky, R. F., Yaqoob, T., Kunieda, H., & Edelson, R. 1996, *ApJ*, 469, 147
- Liu, H., Luo, B., Brandt, W. N., et al. 2021, *ApJ*, 910, 103
- Luo, B., Brandt, W. N., Hall, P. B., et al. 2015, *ApJ*, 805, 122
- Lusso, E., Comastri, A., Vignali, C., et al. 2010, *A&A*, 512, A34
- Lusso, E., Nardini, E., Bisogni, S., et al. 2021, *A&A*, 653, A158
- Marconi, A., Risaliti, G., Gilli, R., et al. 2004, *MNRAS*, 351, 169

- Martocchia, S., Piconcelli, E., Zappacosta, L., et al. 2017, *A&A*, 608, A51
- Marziani, P., del Olmo, A., D’Onofrio, M., et al. 2018, in *Revisiting Narrow-Line Seyfert 1 Galaxies and their Place in the Universe*, 2
- Marziani, P., Martínez Carballo, M. A., Sulentic, J. W., et al. 2016, *Ap&SS*, 361, 29
- Marziani, P. & Sulentic, J. W. 2014, *MNRAS*, 442, 1211
- Marziani, P., Sulentic, J. W., Zwitter, T., Dultzin-Hacyan, D., & Calvani, M. 2001, *ApJ*, 558, 553
- Mason, K. O., Breeveld, A., Much, R., et al. 2001, *A&A*, 365, L36
- Mazzucchelli, C., Bañados, E., Venemans, B. P., et al. 2017, *ApJ*, 849, 91
- Merloni, A., Predehl, P., Becker, W., et al. 2012, arXiv e-prints, arXiv:1209.3114
- Middei, R., Petrucci, P. O., Bianchi, S., et al. 2020, *A&A*, 640, A99
- Mineshige, S., Kawaguchi, T., Takeuchi, M., & Hayashida, K. 2000, *PASJ*, 52, 499
- Miniutti, G., Brandt, W. N., Schneider, D. P., et al. 2012, *MNRAS*, 425, 1718
- Miniutti, G., Fabian, A. C., Brandt, W. N., Gallo, L. C., & Boller, T. 2009, *MNRAS*, 396, L85
- Morabito, L. K., Dai, X., Leighly, K. M., Sivakoff, G. R., & Shankar, F. 2014, *ApJ*, 786, 58
- Nandra, K., George, I. M., Mushotzky, R. F., Turner, T. J., & Yaqoob, T. 1997, *ApJ*, 476, 70
- Nandra, K. & Pounds, K. A. 1994, *MNRAS*, 268, 405
- Nardini, E., Lusso, E., Risaliti, G., et al. 2019, *A&A*, 632, A109
- Nardini, E., Reeves, J. N., Gofford, J., et al. 2015, *Science*, 347, 860
- Ni, Q., Brandt, W. N., Luo, B., et al. 2018, *MNRAS*, 480, 5184
- Ni, Q., Brandt, W. N., Yi, W., et al. 2020, *ApJ*, 889, L37
- Nomura, M., Ohsuga, K., & Done, C. 2020, *MNRAS*, 494, 3616
- Oh, K., Yi, S. K., Schawinski, K., et al. 2015, *ApJS*, 219, 1
- Osterbrock, D. E. & Pogge, R. W. 1985, *ApJ*, 297, 166
- Pâris, I., Petitjean, P., Aubourg, É., et al. 2014, *A&A*, 563, A54
- Petrucci, P. O., Ursini, F., De Rosa, A., et al. 2018, *A&A*, 611, A59
- Piconcelli, E., Jimenez-Bailón, E., Guainazzi, M., et al. 2005, *A&A*, 432, 15
- Planck Collaboration, Ade, P. A. R., Aghanim, N., et al. 2016, *A&A*, 594, A13
- Prevot, M. L., Lequeux, J., Maurice, E., Prevot, L., & Rocca-Volmerange, B. 1984, *A&A*, 132, 389
- Proga, D. 2005, *ApJ*, 630, L9
- Proga, D. & Kallman, T. R. 2004, *ApJ*, 616, 688
- Pu, X., Luo, B., Brandt, W. N., et al. 2020, *ApJ*, 900, 141
- Rakshit, S., Stalin, C. S., & Kotilainen, J. 2020, *ApJS*, 249, 17
- Reeves, J. N., O’Brien, P. T., Braitto, V., et al. 2009, *ApJ*, 701, 493
- Reeves, J. N. & Turner, M. J. L. 2000, *MNRAS*, 316, 234
- Ricci, C., Ho, L. C., Fabian, A. C., et al. 2018, *MNRAS*, 480, 1819
- Richards, G. T., Hall, P. B., Vanden Berk, D. E., et al. 2003, *AJ*, 126, 1131
- Risaliti, G., Young, M., & Elvis, M. 2009, *ApJ*, 700, L6
- Runnoe, J. C., Brotherton, M. S., & Shang, Z. 2012, *MNRAS*, 422, 478
- Schlafly, E. F. & Finkbeiner, D. P. 2011, *ApJ*, 737, 103
- Serafinelli, R., Vagnetti, F., & Middei, R. 2017, *A&A*, 600, A101
- Shakura, N. I. & Sunyaev, R. A. 1973, *A&A*, 500, 33
- Shankar, F., Weinberg, D. H., & Miralda-Escudé, J. 2013, *MNRAS*, 428, 421
- Shemmer, O., Brandt, W. N., Netzer, H., Maiolino, R., & Kaspi, S. 2008, *ApJ*, 682, 81
- Shen, Y. 2013, *Bulletin of the Astronomical Society of India*, 41, 61
- Shen, Y. & Ho, L. C. 2014, *Nature*, 513, 210
- Shirakata, H., Kawaguchi, T., Oogi, T., Okamoto, T., & Nagashima, M. 2019, *MNRAS*, 487, 409
- Sądowski, A., Abramowicz, M., Bursa, M., et al. 2011, *A&A*, 527, A17
- Sądowski, A. & Narayan, R. 2016, *MNRAS*, 456, 3929
- Sobolewska, M. A. & Done, C. 2007, *MNRAS*, 374, 150
- Strüder, L., Briel, U., Dennerl, K., et al. 2001, *A&A*, 365, L18
- Teng, S. H., Brandt, W. N., Harrison, F. A., et al. 2014, *ApJ*, 785, 19
- Toba, Y., Oyabu, S., Matsuhara, H., et al. 2014, *ApJ*, 788, 45
- Tombesi, F., Meléndez, M., Veilleux, S., et al. 2015, *Nature*, 519, 436
- Trakhtenbrot, B., Ricci, C., Koss, M. J., et al. 2017, *MNRAS*, 470, 800
- Turner, M. J. L., Abbey, A., Arnaud, M., et al. 2001, *A&A*, 365, L27
- Vagnetti, F., Antonucci, M., & Trevese, D. 2013, *A&A*, 550, A71
- Vagnetti, F., Turriziani, S., Trevese, D., & Antonucci, M. 2010, *A&A*, 519, A17
- Valiante, R., Agarwal, B., Habouzit, M., & Pezzulli, E. 2017, *PASA*, 34, e031
- Vanden Berk, D. E., Richards, G. T., Bauer, A., et al. 2001, *AJ*, 122, 549
- Vasudevan, R. V. & Fabian, A. C. 2007, *MNRAS*, 381, 1235
- Vestergaard, M. & Peterson, B. M. 2006, *ApJ*, 641, 689
- Vietri, G., Maimieri, V., Kakkad, D., et al. 2020, *A&A*, 644, A175
- Vietri, G., Piconcelli, E., Bischetti, M., et al. 2018, *A&A*, 617, A81
- Waddell, S. G. H. & Gallo, L. C. 2020, *MNRAS*, 498, 5207
- Wu, J., Brandt, W. N., Hall, P. B., et al. 2011, *ApJ*, 736, 28
- Wu, X.-B., Wang, F., Fan, X., et al. 2015, *Nature*, 518, 512
- York, D. G., Adelman, J., Anderson, John E., J., et al. 2000, *AJ*, 120, 1579
- Zappacosta, L., Piconcelli, E., Giustini, M., et al. 2020, *A&A*, 635, L5
- Zubovas, K. & King, A. 2012, *ApJ*, 745, L34
- Zubovas, K. & King, A. 2013, *ApJ*, 769, 51

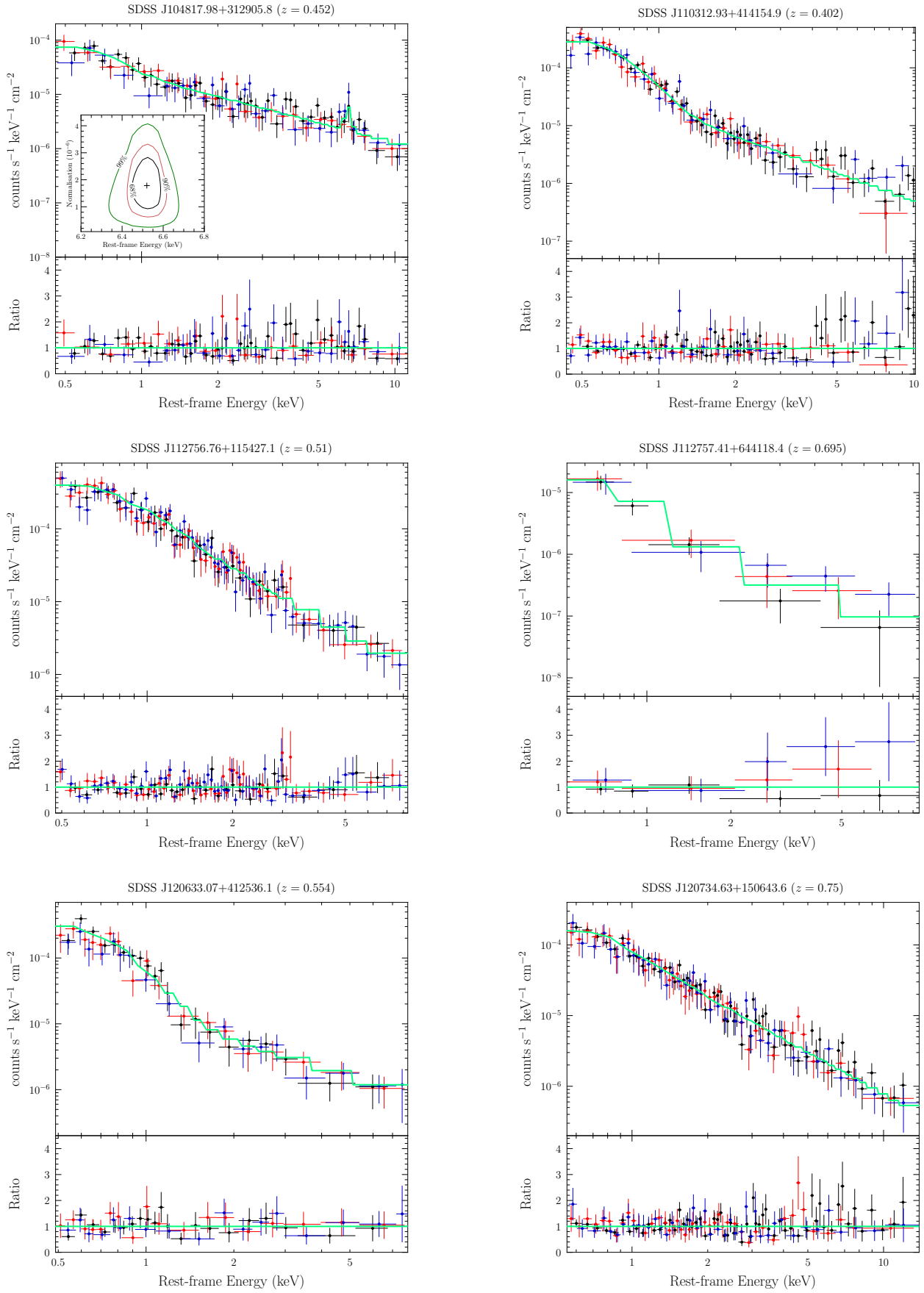
## Appendix A: X-ray spectra of high- $\lambda_{\text{Edd}}$ AGN

Fig. A.1 shows the results of the broadband spectral fits to the EPIC spectrum (pn, MOS1 and MOS2) of the 14 high- $\lambda_{\text{Edd}}$  quasars listed in Tab. 1. The best fit to the bulk of the spectra is provided by a model consisting of a power law and a blackbody component, both modified for Galactic absorption ( $\text{tbabs} \cdot (\text{zpower1w} + \text{zbody})$  in the XSPEC notation).

The only exceptions are J0809+46 and J1048+31. The former shows no excess emission in the soft X-rays where the spectrum, instead, is dominated by an ionised absorption component with high column density (Piconcelli et al., *in prep.*), while the latter requires an additional component (i.e. a Gaussian line) to account for the Fe  $K\alpha$  emission line. Further details on the X-ray spectral analysis can be found in Sect. 3.1.



**Fig. A.1:** (Continued)



**Fig. A.1:** (Continued)

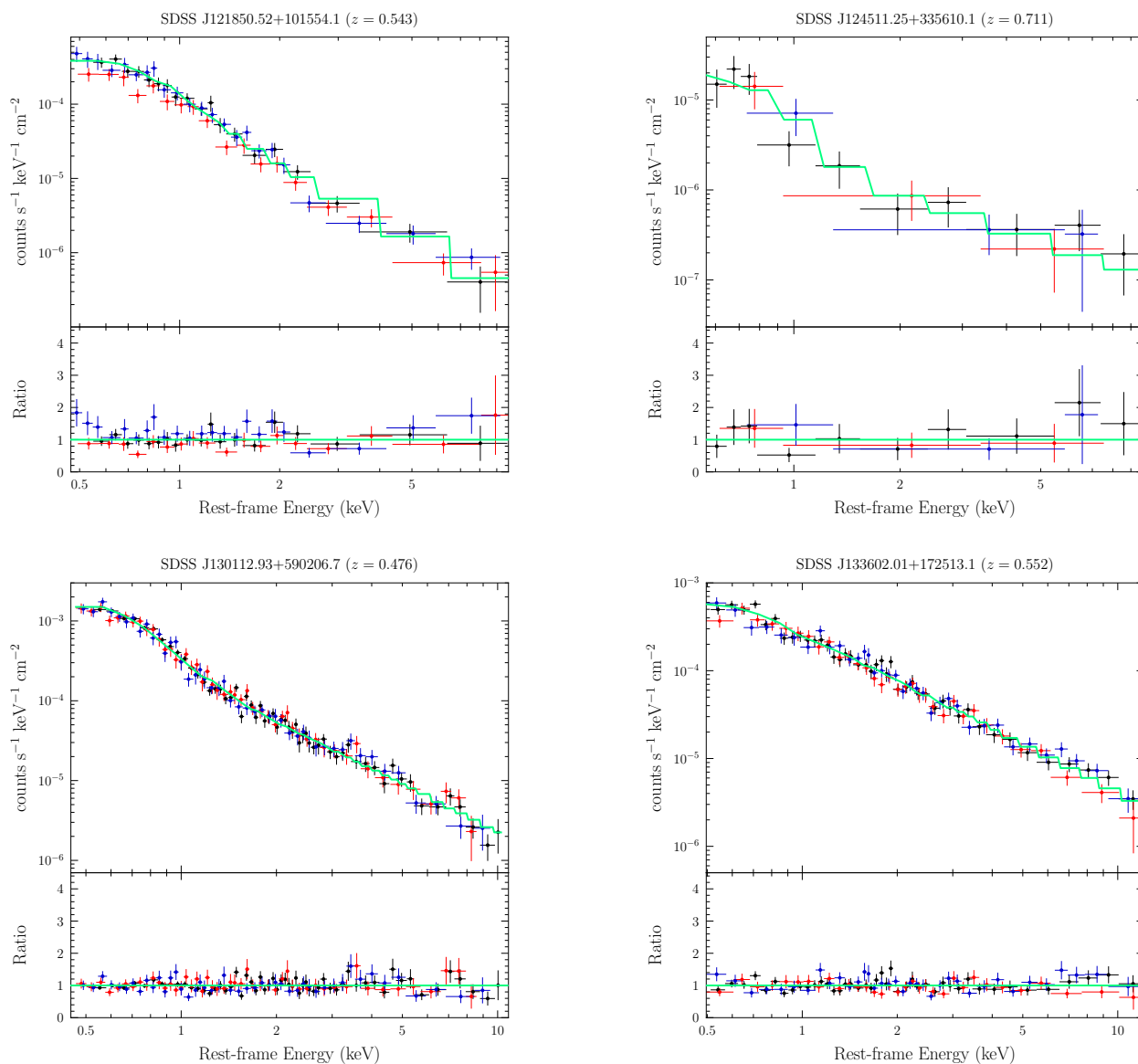


**Fig. A.1:** *XMM-Newton* spectra of the 14 high- $\lambda_{\text{Edd}}$  quasars analysed in this paper. For each source, the top panel shows the X-ray spectrum (data from pn, MOS1 and MOS2 are indicated as black, red and blue points, respectively) and the corresponding best-fit model (green solid line). The bottom panel shows the ratios between the data points and the best-fit model, except for J0809+46, whose spectrum is dominated by an absorption feature in the soft X-rays. To highlight the presence of this component, for this source the extension of the best-fitting hard X-ray continuum power-law model to the soft X-ray portion is shown. Furthermore, for the quasar J1048+31, the inset figure displays the confidence contour plot of normalisation against rest-frame energy of the Gaussian line component which accounts for Fe  $K\alpha$  emission.

## Appendix B: Serendipitous sources

In this section we briefly summarise the results of the X-ray spectral analysis of a small group of serendipitous X-ray sources with interesting X-ray properties and AGN optical classification available from the literature, located in the *XMM-Newton* field of view of our targeted high- $\lambda_{\text{Edd}}$  AGN. Figure B.1 shows their X-ray spectra along with the corresponding best fit model.

*SDSS J120753.12+150221.2*. This source is an X-ray bright Seyfert 1 galaxy at redshift  $z = 0.08558$  (Oh et al. 2015). Its X-ray spectrum is characterised by a soft excess with  $R_{\text{S}/\text{P}} = 0.16$ . The broadband ( $E = 0.3 - 10$  keV observer frame) continuum is well described by a power law ( $\Gamma = 2.06 \pm 0.06$ ) modified by Galactic absorption, plus a blackbody component ( $kT = 120_{-20}^{+10}$  eV). In the  $2 - 10$  keV energy interval, we measure a flux  $F_{2-10} \sim 10^{-12}$  erg  $\text{cm}^{-2}$   $\text{s}^{-1}$  and a luminosity  $L_{2-10} \sim 1.9 \times 10^{43}$  erg  $\text{s}^{-1}$ . The net pn/MOS1/MOS2 photon counts in the broadband  $E = 0.3 - 10$  keV observer-frame energy interval are 6098/2060/1963.

*2MASX J12071559+1512158*. This source is classified as a Seyfert 1 galaxy (Toba et al. 2014) at redshift  $z = 0.10701$ . Its soft X-ray spectrum is characterised by absorption below 1 keV rest frame. A good fit of the broadband continuum consists of a power law component with  $\Gamma = 1.8 \pm 0.2$ . The absorption feature in the soft X-rays is modelled with a photoelectric absorber (zwaabs component in XSPEC) with a column density of  $N_{\text{H}} = (0.7 \pm 0.2) \times 10^{22}$   $\text{cm}^{-2}$ . The source has a flux  $F_{2-10} \sim 5.7 \times 10^{-13}$  erg

$\text{cm}^{-2} \text{s}^{-1}$  and a luminosity  $L_{2-10} \sim 1.6 \times 10^{43} \text{ erg s}^{-1}$ . The net pn/MOS1/MOS2 photon counts in the broadband  $E = 0.3 - 10 \text{ keV}$  observer-frame energy interval are 859/397/362.

*SDSS J094012.29+461850.3*. This QSO is located at redshift  $z = 0.7112$  (P aris et al. 2014). To fit the X-ray broadband continuum, we first considered a simple model consisting of a power law modified by Galactic absorption. However, such a model resulted in a poor fit of the underlying continuum. We suspected the discrepancy could arise from the deficit below 2 keV rest frame. So we included a partial covering, cold absorption component in the model. The covering factor and column density measured with *XMM-Newton* are  $C_f = 0.7^{+0.1}_{-0.2}$  and  $N_H = 1.7^{+1.5}_{-1.1} \times 10^{22} \text{ cm}^{-2}$ , respectively. The primary continuum is described by a power law with photon index  $\Gamma = 1.4 \pm 0.3$ . We estimate a flux  $F_{2-10} \sim 7.1 \times 10^{-14} \text{ erg cm}^{-2} \text{ s}^{-1}$  and a luminosity  $L_{2-10} \sim 1.2 \times 10^{44} \text{ erg s}^{-1}$ . The net pn/MOS1/MOS2 photon counts in the broadband  $E = 0.3 - 10 \text{ keV}$  observer-frame energy interval are 104/42/64.

*SDSS J120558.16+412825.3*. This source is a Seyfert 1 galaxy at redshift  $z = 0.22648$  (Toba et al. 2014). The *XMM-Newton* data do not require the presence of a soft excess and a model consisting of a power law, modified by Galactic absorption, with photon index  $\Gamma = 1.8 \pm 0.2$  provides a best fit to the X-ray spectrum. We estimate a flux  $F_{2-10} \sim 1.2 \times 10^{-13} \text{ erg cm}^{-2} \text{ s}^{-1}$ , which implies a luminosity  $L_{2-10} \sim 1.8 \times 10^{43} \text{ erg s}^{-1}$ . The net pn/MOS1/MOS2 photon counts in the broadband  $E = 0.3 - 10 \text{ keV}$  observer-frame energy interval are 121/96/53.

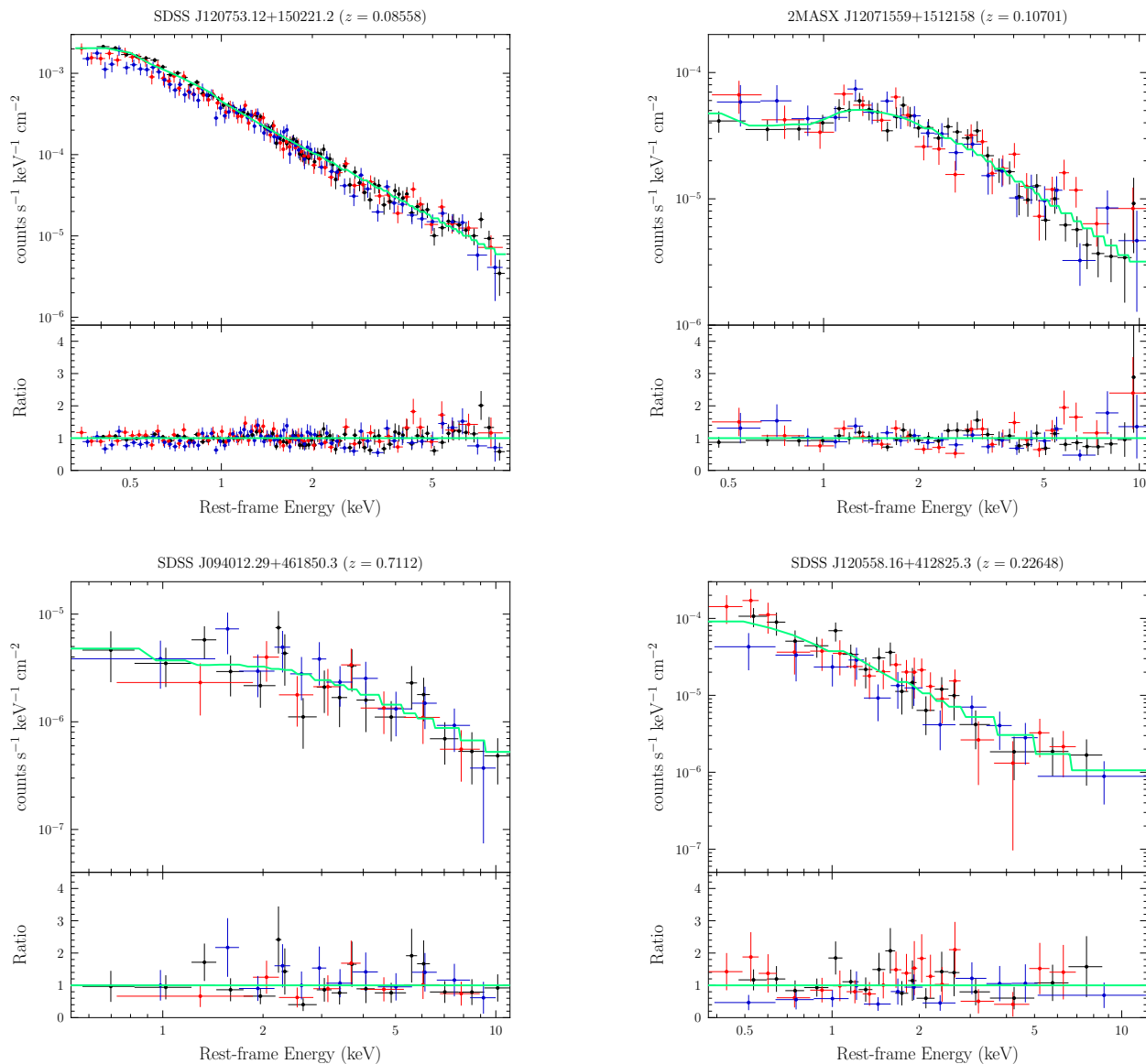


**Fig. B.1:** *XMM-Newton* spectra of the serendipitous sources described in Appendix B, with their corresponding best fit. Each top panel shows the X-ray spectrum and the best-fit line (in green). Each spectrum is rebinned for plotting purposes only. The bottom panels describe the ratio between the data points and the best-fit model. Data from EPIC-pn, MOS1 and MOS2 are shown in black, red and blue, respectively.